12-2017

The Development of Cesium Calcium Bromo-Iodide scintillator for X-ray and Gamma ray detection

Matthew Starr Loyd
University of Tennessee, Knoxville, mloyd1@vols.utk.edu

Recommended Citation

Loyd, Matthew Starr, "The Development of Cesium Calcium Bromo-Iodide scintillator for X-ray and Gamma ray detection. " Master's Thesis, University of Tennessee, 2017.
https://trace.tennessee.edu/utk_gradthes/4954

To the Graduate Council:

I am submitting herewith a thesis written by Matthew Starr Loyd entitled "The Development of Cesium Calcium Bromo-Iodide scintillator for X-ray and Gamma ray detection." I have examined the final electronic copy of this thesis for form and content and recommend that it be accepted in partial fulfillment of the requirements for the degree of Master of Science, with a major in Nuclear Engineering.

Charles L. Melcher, Major Professor

We have read this thesis and recommend its acceptance:

Mariya Zhuravleva, Jason Hayward

Accepted for the Council:
Carolyn R. Hodges

Vice Provost and Dean of the Graduate School

(Original signatures are on file with official student records.)

The Development of Cesium Calcium Bromo-Iodide scintillator for X-ray and Gamma ray detection

A Thesis Presented for the

Master of Science

Degree

The University of Tennessee, Knoxville

Matthew Starr Loyd

December 2017

Acknowledgements

The work presented in this thesis is not only my work, but a result of a collaboration of effort by many people, who I would like to thank here. First and foremost, I would like to thank my advisors Dr. Charles Melcher and Dr. Mariya Zhuravleva, who have guided me since my start at the SMRC, and have also been extremely patient with me. This includes Merry Koschan, who has personally improved my writing and presenting style, as well as offering wonderful suggestions on how to lead my research. I would also like to thank Dr. Jason Hayward for taking time to be on my committee. I would not have been able to accomplish this without the teachings of my lab mentors and friends Adam Lindsey, Luis Stand, Yuntao Wu, and Will McAlexander. I would also like to thank Camera Foster for helping me pass all my classes the last six years. Additionally, this work was finished in a timely manner due to assistance from Undergraduate students Alyssa Lindsey, Noah Schaftlein, Kevin Macdonald, Daniel Rutstrum, and Jesse Johnson. The lab would not be able to operate without the amazing help of Doug, who makes stuff, and Frank and Randy, who get stuff. I would also like to thank the ladies of the Ferris office: Tracy, Tonya, Martha, and Carla, for making my travel and everything administrative a breeze.

None of this would be possible without the incredible support from my parents, who worked hard to ensure I would have this opportunity, and my brother and sister, for keeping me grounded and always being my friends. Finally, I would like to thank my fiancé Sydney for being my best friend and putting up with my late night and weekends at the lab, and providing me with motivation to work hard and persevere.

Abstract

$CsCaI_3$:Eu [cesium calcium iodide doped with europium] is a promising scintillator material that can be grown from the melt, but undergoes a tetragonal to orthorhombic phase transition upon cooling at 255 °C [degrees Celsius], causing twinning and cloudiness. The purpose of this work is to suppress this solid to solid phase transition in the $CsCaI_3$:Eu scintillator, which has a light yield of ~40000 ph/Mev and energy resolution at 662keV of ~4%, by halide replacement to form the compound $CsCaBr_xI_{3-x}$:Eu [cesium calcium bromo-iodide doped with europium]. Crystals 8 cm^3 [cubic centimeters] in volume were grown using the vertical Bridgman method with varying bromine replacement from x=0.2 to x=1, resulting in improved transparency for crystals with bromine content x > 0.6. Powder X-ray diffraction data coupled with differential scanning calorimetry and radioluminescence measurements were used to investigate structural modifications, melting point dependence and spectral emission dependence on the bromine/iodine ratio. Partial replacement of iodine by bromine improves optical quality and scintillation properties by stabilizing the structure, rendering it useful for isotope identification for national security applications. The composition $CsCaBr_{0.8}I_{2.2}$:Eu [cesium calcium bromo (0.8) iodide (2.2) doped with europium] was determined to be the best combination of improved structure and performance, and larger 22 and 38 mm Ø [diameter[crystals were grown for further evaluation. Large size slabs showed good crystal quality and improved performance over $CsCaI_3$Eu with 8.4% and 9.5% energy resolution at 662 keV, respectively. The improved performance this composition over $CsCaI_3$:Eu introduces the possibility of its use for gamma spectroscopy in national security applications.

Table of Contents

List of Tables

List of Figures

Chapter 1
Scintillators as Gamma and X-ray detectors

1.1 Radiation detection for national security

Ever since the United States' usage of two nuclear weapons at the end of World War II, much emphasis has been placed on preventing nuclear war due to the catastrophic and apocalyptic outcomes. Although nuclear war is currently prevented due to mutual destruction, there is always the threat of a rouge state or individual obtaining, or in the worst-case scenario, detonating a nuclear weapon. Because of this, nuclear material for military or commercial use is heavily safeguarded and accounted for. In spite of this, only relatively small amounts of fissionable materials are required for production of a nuclear warhead. The International Atomic Energy Agency (IAEA) lists a significant quantity of high-enriched uranium (HEU) at 25 kg and plutonium at 8 kg [1]. Being able to detect trace amounts of certain radio-isotopes, such as ^{235}U, ^{233}U, and ^{239}Pu, is a major asset to non-proliferation. Fortunately, these materials have very distinct electromagnetic signals due to their radioactivity. The radioactive decay of unstable isotopes can result in emission of both Gamma (γ) rays from the de-excitement of a decayed nucleus, and X-rays from the transition of electrons from higher to lower energy shells. Decay can also produce alpha (α) and beta (β) particles and neutrons, but alphas and betas can be easily shielded, while neutrons require certain isotopes (namely, ^{6}Li or ^{10}B) to be detected by scintillators, therefore are not the focus of this work.

Gamma and X-rays are both on the electromagnetic spectrum with energies above that of visible light. Characteristic X-rays produced from excitation via decay range from hundreds of eV's to tens of keV's, while gamma rays from radioactive decay can range from tens of keV's to a few MeV's. Both X-rays and gammas are emitted as monoenergetic photons, which aids in the identification of their source isotopes. For instance, ^{137}Cs, a fission product and common research isotope, emits 661.7 keV gammas following β-decay, as well as 32 keV X-rays due to K-shell electrons ejected via internal conversion. A correctly measured 661.7 keV gamma can with great certainty identify the presence of ^{137}Cs.

Once emitted from the source, gammas and X-rays will travel until interacting with matter. The intensity of a beam of photons at a distance x through a material with a linear attenuation coefficient μ is given by:

$$I = I_0 e^{-\mu x} \tag{1}$$

The linear attenuation coefficient is a sum of three types of interactions with materials: photoelectric effect, Compton scattering, and pair production. These are stochastic events, with the probability of interaction dependent on the atomic number (Z) and density (ρ) of the material, as well as the energy of the photon. The photoelectric effect is the total absorption of a photon into a material, resulting in an electron with the energy of the photon, minus the binding energy of the electron, which is fairly small compared to the typical gamma energies. Compton scattering occurs when a photon inelastically scatters off a rest electron in the material, deposits a portion of its energy to the electron, and is deflected by some angle θ. Finally, pair production is when a gamma converts into an electron and a positron. This can only occur above 1.022 MeV, which is twice the rest mass of an electron. For most of the gamma energies for non-proliferation concerns, Compton scattering and photoelectric effect dominate. Figure 1 plots the linear attenuation and energy-absorption coefficients of water (an analoug for human tissue) as a function of photon energy.

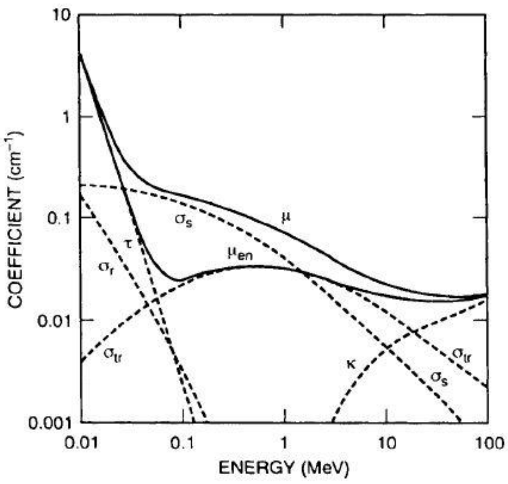

Figure 1: Linear attenuation and energy absorption coefficients for photons in water [2] showing the change in photon interaction as a function of energy.

There are three main challenges when using radiation to discover hidden, illicit radioactive materials: detecting, locating, and identifying. Detecting radiation is typically done with permanent detectors placed at areas of concern, such as airports and border crossings. Locating radiation requires pinpointing a location using scanning with handheld detectors or deployment of complex devices such as a Compton camera. Identifying is more difficult, but can be accomplished with techniqures such as gamma spectroscopy. This requires some proportional response regarding incoming particle energy, as well as a high enough resolution to differentiate between similar energy sources. For identifying gamma and X-ray energies, the most widely deployed options are solid-state detectors, which include semiconductors (both cooled and room temperature) and scintillators, the latter which will be discussed in detail in this work.

1.2 Scintillator Detectors

Solid-State detectors rely on the production of electron-hole pairs to measure the energy of an incoming particle. If the incoming radiation has sufficient enough energy to ionize the detector, a certain number of valence electrons will be excited into the conduction band. This number is proportional to the total energy that the particle deposited into the device. Semiconductors collect this information by using a bias to convert the electron hole pairs into an electrical signal, while scintillators allow them to recombine, and in the process emitting visible light. Often this process is made more efficient by purposefully adding a small impurity concentration, called a dopant or activator. Figure 2 highlights the scintillation process in a doped material.

The number of visible photons created from a certain amount of deposited energy is referred to as the light yield, and is described by the following equation: [3, 4]

$$n_p = \frac{E_\gamma}{2.3E_g}\beta SQ \tag{2}$$

where E_g is the band gap energy and β, S, and Q are efficiency factors for conversion, transfer, and luminescence, respectively. Once the light is emitted, it is collected by a photo-sensitive detector, most often a photomultiplier tube (PMT), a vacuum tube that converts photons into electrons using a photocathode, then multiplies them via a series of dynodes. The PMT outputs an electronic signal, which can be sent through a multi-channel analyzer (MCA). The result is a histogram of different signal intensities, called the pulse height spectrum. Figure 3 shows a typical ^{137}Cs pulse height spectrum measured with a scintillator detector: NaI doped with thallium. The spectrum includes not only the full deposition 662 keV peak, but also the full Compton spectrum, which results from a photon Compton scattering and leaving the scintillator after only depositing a portion of its energy. The full deposition peak is characterized by its Gaussian distribution and energy resolution, which is the full width at half maximum divided by the centroid energy. The energy resolution at 662 keV is often used as a figure of merit for the performance of a scintillator.

The energy resolution of a crystal scintillator can be separated into three contributors shown below [5].

$$R^2 = R_{stat}^2 + R_{in}^2 + R_{np}^2 \tag{3}$$

The quantity R_{stat} is the contribution from the photon counting statistics, and is a function of the crystal light yield and a PMT multiplication variance factor [6]. The quantity R_{in} originates from the inhomogeneity in both the production and collection of light within the scintillator. Finally, R_{np} is the

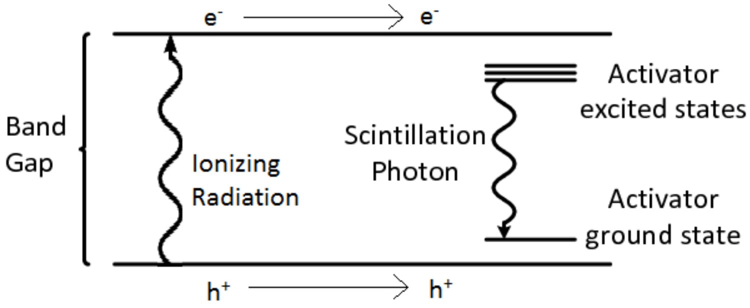

Figure 2: Scintillation mechanism in a doped scintillator [7].

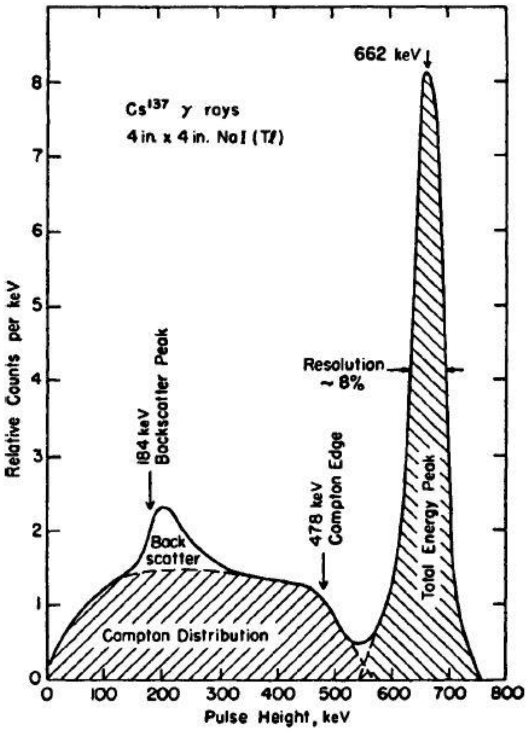

Figure 3: Pulse Height Spectrum from a NaI:Tl Scintillator irradiated with a ^{137}Cs source [2].

.

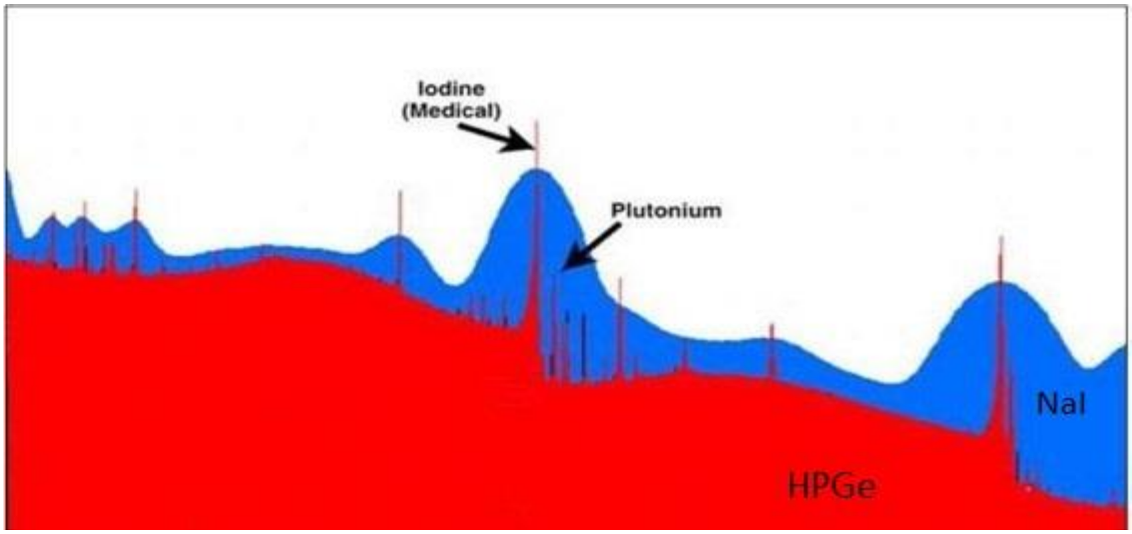

Figure 4: Pulse Height Spectrum comparing resolutions HPGe (red) and NaI:Tl (blue) [8].

non-proportionality contribution, which accounts for the variation in light yield as measured at different energies. Figure 4 highlights the importance of energy resolution by comparing the same spectrum measured with two different detectors: NaI:Tl and high purity germanium (HPGe) semiconductor. It can be easily seen that although the HPGe has a fine enough resolution to differentiate between medical Iodine and Plutonium, the NaI:Tl does not. However, NaI:Tl is orders of magnitude less expensive to produce, and can be utilized at room temperature. Additionally, much can be determined with even a moderate resolution when a good data analysis algorithm is utilized. In order for a scintillator to be the most useful for spectroscopy, it must meet certain engineering requirements such as high sensitivity and strong resolution. Therefore, the ideal gamma sensitive scintillator will have a high density and effective atomic number, light yield, and energy resolution, in addition to being producible at large sizes and low costs.

Chapter 2

$CsCaI_3$:Eu

2.1 Metal Halide Scintillator

In the last two decades, one type of scintillators has been a focus of gamma spectroscopy for national security applications: non-organic metal-halide single crystals. These compositions have several advantages over plastic and oxide scintillation materials such as high density and impressive performance [9]. Additionally, they have melting temperatures (<1000°C) much lower than oxide alternatives [10], allowing for simpler crystal growth methods. Although NaI doped with thallium and CsI doped with thallium or sodium [11, 12] have been used as scintillators for some time now, more recent compositions such as SrI_2:Eu [13], $LaBr_3$:Ce [14], $Ba(Br,I)_2$:Eu[15] and $CeBr_3$ [16] have been developed extensively due to their high light yield (>60,000 ph/MeV) and high resolutions (<3% E.R. at 662 keV). Sequentially, europium-doped ternary alkali/alkali-earth/halide materials have been explored resulting in compositions such as $KCaI_3$:Eu[17] , KSr_2I_5:Eu[18] , $CsSrBr_3$:Eu[19], and KBa_2I_5:Eu [20]. Although metal halides have many advantages, one main disadvantage is their tendency to be hygroscopic, which requires additional handling and containment constraints.

These materials are typically produced via the vertical Bridgman-Stockbarger method of single crystal growth [21, 22] due to its relative simplicity and its suitability for growth of metal halides. This method consists of a vertical tube furnace with at least two zones, heated via resistance coils and controlled with embedded thermocouples. The crystal starts in the upper zone above the material melting point, then is lowered into the bottom zone, below the melting temperature. An insulated separator is often used to increase the thermal gradient between the hot and cold zones [23, 24]. Because of the hygroscopicity of metal halides, the starting materials are typically loaded into a vacuum sealed quartz ampoule to prevent exposure to moisture.

2.2 Size deterioration of scintillator performance

National security applications require scintillator crystals in sizes large enough to have decent efficiency. For instance, some handheld detectors for spectroscopic applications utilize a 1" square cylinder of NaI:Tl. During the discovery phase of new metal halide scintillators, high quality crystal growth at 1" or greater diameters can be difficult, making the growth process the limiting factor in deploying new compositions. However, this has been achieved for many of the previous materials, and there are secondary factors that hinder performance at large sizes past the successful growth. The optical quality of the crystal needs to be pristine in order to maximize collection of scintillation photons. In general, slower growth rates can improve the crystal quality by preventing incorporation of defects and unwanted impurities.

Europium doping of certain compositions can also introduce spectroscopic performance issues at large crystal sizes. For compositions that substitute europium for strontium, such as SrI_2:Eu and KSr_2I_5:Eu, dopant segregation should be minimized due to the similar atomic radius of europium and strontium [25-27]. However, materials that utilize calcium as the divalent cation are more prone to segregation [28]. This can lead to a variance of activator compositions across the boule, thereby increasing the R_{in} aspect of energy resolution. Another issue with europium doped crystals that is exaggerated with size is self-absorption. When the stokes shift as measured via photoluminescence is relatively small and there is some overlap between the excitation and emission spectra of europium doped scintillators, there is probability that some of the emitted photons will re-excite the crystal. This effect has been shown to increase the scintillation decay time of these crystals, and is exaggerated at larger crystal sizes and europium concentration [29]. However, a low europium concentration such as 0.5% can help mitigate these effects [30, 31].

2.3 Properties of $CsCaI_3$:Eu

$CsCaI_3$:Eu is a promising scintillator composition, with a light yield of 40,000 ph/MeV and an energy resolution of ~4% at 662 kev, measured on small size crystals [32]. Additionally, it has a suitable density (4.06 g/cm^3) [33] for national security applications. Large sized boules of $CsCaI_3$:Eu have been grown successfully and repeatedly without cracking, as shown in Figure 5. As can be seen below, $CsCaI_3$:Eu has a cloudy, translucent appearance, which becomes more visible at larger sizes. This cloudiness can lead to light scattering in the crystal, which increases the probability of self-absorption. Figure 6 highlights this effect by comparing the performance of different size crystals of $CsCaI_3$:Eu. Both the light yield and energy resolution are worsened as the volume of the crystal increases.

The source of this non-optimal crystal quality is most likely caused to stress introduced due to a solid-to-solid phase transition that $CsCaI_3$:Eu undergoes upon cooling. This is observed via a differential scanning calorimetry (DSC) measurement, in which a pair of exothermic and endothermic peaks are visible around 250°C, highlighted in Figure 7. The composition crystalizes into a tetragonal lattice, then transforms into an orthorhombic structure [32, 34]. This transition is explored more later in this work. Polarized light imagery on room temperature crystals has revealed the presence of a twinned microstructure. Twinning as a stress release mechanism has been observed in similar perovskite structures that undergo a tetragonal to orthorhombic phase transition [35].

Structurally, $CsCaI_3$:Eu at room temperature is in stark contrast to $CsCaBr_3$:Eu and $CsCaCl_3$:Eu, which have cubic crystal structures and lack the cloudy appearance of $CsCaI_3$:Eu [33, 36]. A cubic crystal structure is more favorable for crystal growth, and the anisotropy can reduce variations due to thermal expansion and index of refraction compared to non-cubic crystals. The room temperature structure of a ABX_3 perovskite crystal can roughly be predicted using a ratio of the ionic radii of its different elements known as the Goldschmidt tolerance factor [37]:

$$t = \frac{r_A + r_x}{\sqrt{2}(r_B + r_x)} \tag{4}$$

A perovskite with a t value closer to 1 is more likely to be cubic at room temperature, with decreasing t values resulting in tetragonal and orthorhombic structures. The bromide and chloride compositions both have greater tolerance factors than the iodine. However, both have significantly worse light yield and energy resolution than $CsCaI_3$:Eu. Table 1 compares scintillation and material property values of $CsCaX_3$:Eu (X= I,Br,Cl). The effective atomic number (Z_{eff}) for a compound with n components was calculated using the following equation first described by Murty [38]:

$$Z_{eff} = \sqrt[2.94]{\sum_{i}^{n} f_i Z_i^{2.94}} \tag{5}$$

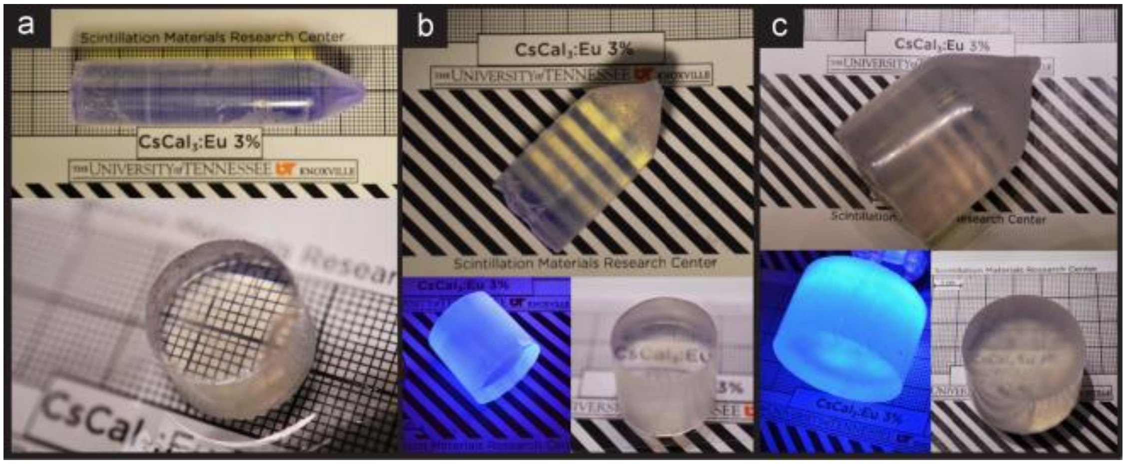

Figure 5: Single crystal boules of $CsCaI_3$:Eu at Ø 15 mm (a), Ø 22 mm (b) and Ø 35 mm (c). The transparency of the material degrades as the thickness of the boule increases.

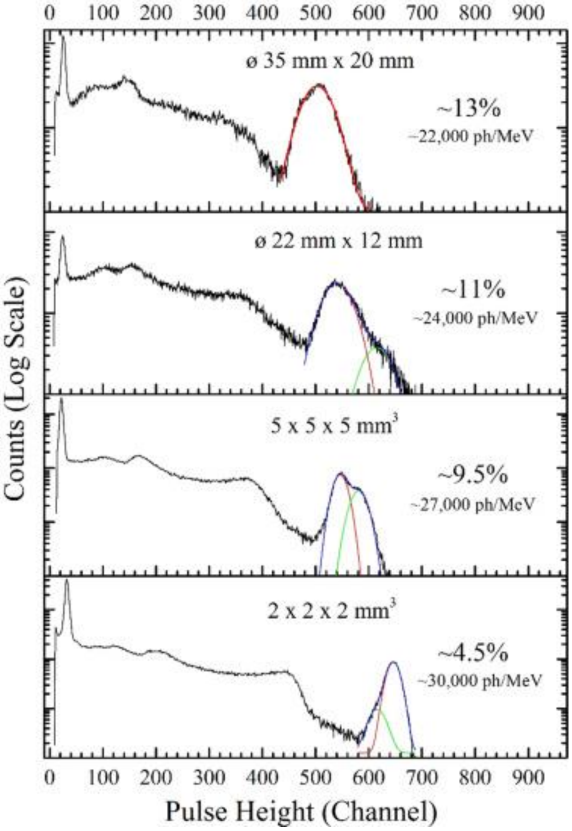

Figure 6: ^{137}Cs Spectra for various size crystals of CsCaI$_3$:Eu [32]. The performance of CsCaI$_3$:Eu degrades as the sample size increases.

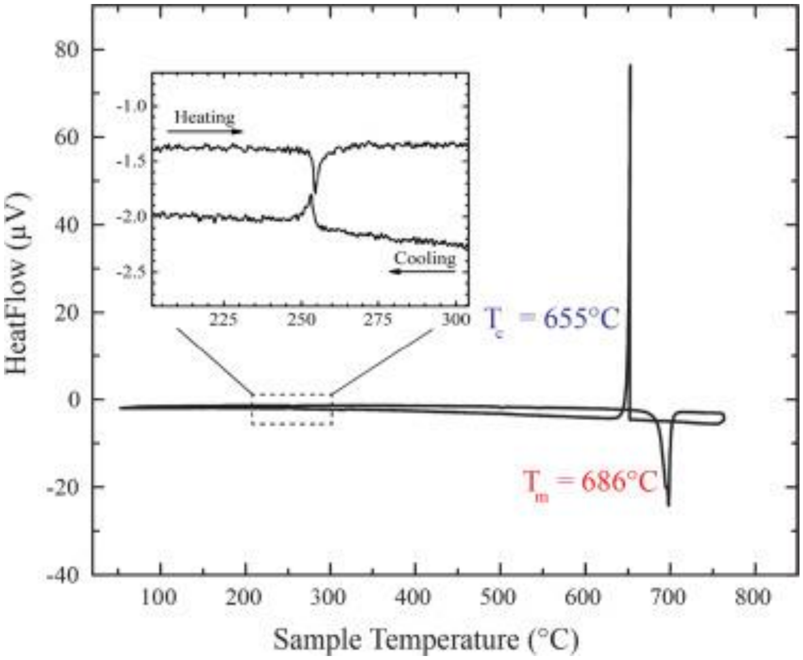

Figure 7: Differential Scanning Calorimetry curve of $CsCaI_3$:Eu, with phase transition enlarged.

Table 1: Scintillation and material properties of $CsCaX_3$:Eu scintillators

Property	$CsCaI_3$:Eu	$CsCaBr_3$:Eu	$CsCaCl_3$:Eu
Light Yield (ph/MeV)	40,000	28,000	18,000
Energy resolution at 662 keV	~4%	9.3%	8.9%
Density (g/cm^3)	4.06	3.72	3.00
Z_{eff}	52.0a	42.4	42.2

where f_i is the fraction of total electrons contributed by element i, and Z_i is the atomic number of element i. It can be readily seen that as the halide element decreases in Z, the density, Z_{eff}, and light yield also decrease. It is difficult to attribute the change in energy resolution to the composition change alone, as crystal quality is a major factor.

While changes in the physical properties of the ternary compositions are easy to understand, variations in the scintillation properties are harder to reconcile. Decreased light yield in the I>Br>Cl direction has been observed in other halide materials such as $CsSrX_3$:Eu [39, 40] and KSr_2X_5:Eu [41], as well as mixed halide compositions such as $CeCl_xBr_{3-x}$ [42]. This trend can be generally attributed to an increase in band gap as a result of the increase of the electron affinity as one moves from iodine up to chlorine [43].

Although a full switch of iodine for bromide significantly reduces the properties of $CsCaX_3$:Eu, a partial substitution could change the room temperature structure of $CsCaI_3$:Eu while still maintaining high spectroscopic performance. Additionally, certain mixed halide crystals have been produced with a higher light yield than the two single halide compositions [44]. Figure 8 shows the calculated Goldschmidt tolerance factor for $CsCaI_{3-x}Br_x$. By substituting bromine, it is possible to achieve the goal of this research of improving the optical quality of $CsCaI_3$:Eu, while maintaining high light yield and energy resolution, thus rendering it useful for national security applications.

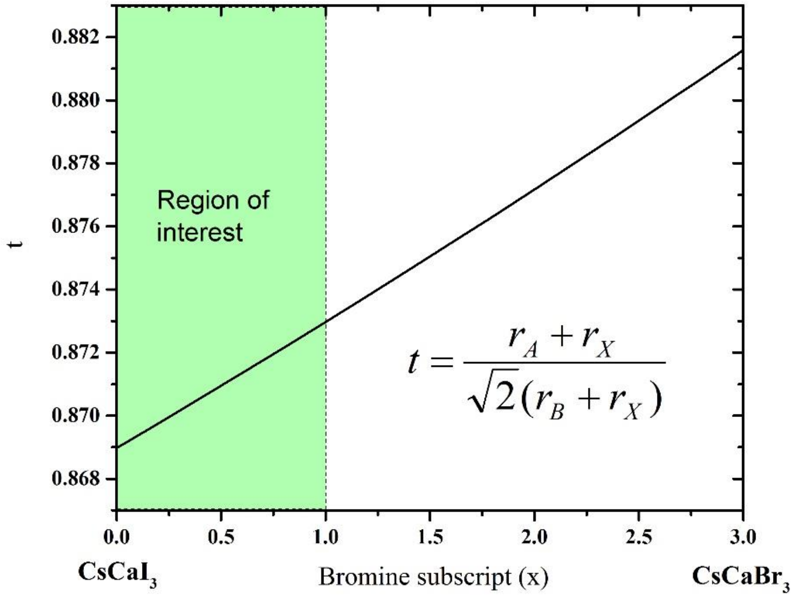

Figure 8: Goldschmidt tolerance factor for $CsCaX_3$ (I,Br) and the region of interest for this work.

Chapter 3

Experimental Methods

3.1 Structural analysis of $CsCaI_3$:Eu

Before changing the composition of $CsCaI_3$:Eu to improve its structure, a better understanding of its multiple structures and the transition between them is required. For this reason, high temperature X-ray diffraction (HTXRD) was measured on powdered samples. Due to the hygroscopic nature of this composition, special procedures were taken during preparation, handling, and measurement to ensure pristine results. All raw materials for this work were purchased from APL or Sigma Aldrich and were in the form of anhydrous beads with purity levels of 99.99% or greater. The crystals for powder diffraction were prepared inside of a nitrogen purged glovebox with less than 1 ppm oxygen and moisture. Starting materials of CsI, CaI_2, and EuI_2 were loaded into a quartz ampoule with a ratio of 1:0.95:0.05 for a nominal 5% dopant concentration. The ampoule was then evacuated to a pressure of no more than 10^{-6} Torr. During the evacuation, the material was heated to 200°C to fully remove any trace moisture from the beads or the ampoule. The ampoule was then sealed under vacuum with a hydrogen-oxygen torch.

Crystal growth was accomplished inside of a transparent furnace with a thermal gradient of 25°C/cm at the solid-liquid interface, which was achieved by utilizing a thermal insulating “donut” to separate the top and bottom zones. The crystal was translated downward at a speed of 1 mm/hr, and cooled to room temperature at 10 °C/hr. The grown crystal was then taken back into a nitrogen drybox and removed from its ampoule. Pieces of the crystal were broken and powdered via mortar and pestle. Finally, the powder sample was loaded onto a Ø15 mm x 0.4 mm alumina sample holder and transferred to the HTXRD instrument.

The sample was housed inside of an Anton-Parr HTK 1200N high temperature oven during measurement, which was evacuated to below 10^{-7} torr. The sample was measured with a Panalytical Empyrean diffractometer in the Bragg-Brentano geometry. Cu K_α X-rays were generated at 45kV and 40 mA. On the incident beam side, a 0.04 rad soller slit, a 0.125°divergence slit, a 0.25° anti-scatter slit, and a 10 mm beam mask were used. A PIXcel3D-Medipix 3 area detector operated in 1D scanning mode was used on the diffracted beam, with 0.04 rad roller slits, a 5 mm fixed anti-scatter slit, and a 0.020 mm nickel beta filer. Each scan ran from 10-70° 2θ with a step size of 0.013° and total scan time of about 30 minutes. Scans were taken at different temperatures selected to best highlight the phase transition. A heating rate of 5 °C/min was used between scans to reach the desired temperatures.

Analysis of the powder diffraction spectra was carried out with GSAS II, an open-source software package for Reitveld refinement [45]. For the low temperature phase, the published orthorhombic Pnma structure with lattice parameters: a = 8.6226 Å, b = 12.282 Å, and c = 8.555 Å were used as a starting point for refinement. A phase search was carried out for the peaks found in the high temperature phase, and the best match was found to be a tetragonal P4/mbm phase with lattice parameters a = 8.772 Å and c = 6.260 Å. Least Squares refinement was done sequentially, starting with the lowest measured temperature for each phase. A LaB_6 sample was measured in the same method to derive instrumental parameters to be used for refinement of $CsCaI_3$:Eu. Thermal expansion coefficients were calculated for the lattice parameters that varied linearly with temperature by dividing the change in length by the temperature range and the average length over said range.

3.2 Crystal growth of $CsCaBr_xI_{3-x}$:Eu

Before growing large size crystals of $CsCaBr_xI_{3-x}$:Eu, the optimal bromine concentration must be explored. The goal is to find a composition that has improved optical quality over $CsCaI_3$:Eu, while still maintaining high light yield and energy resolution. Anhydrous, beaded CsI, CsBr, CaI_2, and EuI_2 with trace metal concentrations less than 0.01% were used for synthesis of $CsCaBr_xI_{3-x}$:Eu. For the search of an optimal bromine concentration, five samples with x= 0.2, 0.4, 0.6, 0.8, and 1 were prepared. A dopant concentration of 7% europium in calcium sites was used for each crystal. Starting materials were loaded into Ø 15 mm self-seeding quartz ampoules inside a nitrogen drybox and dried under evacuation at 250°C. Ampoules were then sealed at a pressure of $<10^{-6}$ torr.

The four samples with x= 0.2-0.8 were grown in a vertical Bridgman multi ampoule growth station (MAGS) completely designed and build in house at the University of Tennessee. This furnace has been used successfully to grow up to 5 multiple crystals of $CsCaI_3$:Eu [46]. The current set up however only allows for 4 crystals to be grown simultaneously. A schematic of the furnace is shown in Figure 9. Ampoules were loaded into the mullite bays, then surrounded by beaded alumina insulation to ensure stability and thermal protection from variations in the furnace. The furnace was heated to a temperature of 800 °C for 12 hours to ensure complete mixing of starting materials, then cooled to zone temperatures of 760 °C and 530 °C. All four bays were translated downward at a speed of 1 mm/hr until the entire charge was solidified. The furnace was then cooled to room temperature at 7 °C/hr.

The final x=1 crystal was grown in a single bore, 24-zone vertical Bridgman furnace with a temperature profile similar to the one in MAGS. The same heating, translation, and cooling profile was used to eliminate as much variation as possible. All five crystals were transferred into a drybox and removed from their ampoules. To mitigate effects of variation from crystal quality due to growth, a 5 mm slab was cut from the cone region of each crystal, which were generally free from inclusions. This was accomplished inside the drybox with a diamond impregnated wire saw. These slabs were then polished using successive 600, 800, and 1200 grit polishing papers and lapping oil to ensure an visibly smooth surface for characterization.

Crystals of the better compositions were grown at Ø 22 mm and Ø38 mm using a transparent growth furnace to ensure a flat growth interface. Additionally, a Ø 22 mm crystal with a reduced europium concentration was grown in a carbon coated ampoule in an attempt to mitigate self-absorption effects and prevent surface cracking. These crystals were cut and polished in a similar method.

3.3 Characterization

3.3.1 Physical Properties

Differential Scanning Calorimetry

Differential Scanning Calorimetry (DSC) was used to determine melting temperatures, phase transitions, and the presence of multiple phases. A Labsys Evo TG-DSC instrument with a maximum temperature of 1600 °C was used to carry out this measurement. A DSC works by heating up a sample and recording the energy required to raise its temperature as compared to a reference. More heat is required to raise the temperature of a material during an endothermic reaction, such as melting, while less heat is required during exothermic processes such as crystallization. These, as well as phase transitions, will be recorded on a DSC scan, such as the one for $CsCaI_3$:Eu in Figure 7.

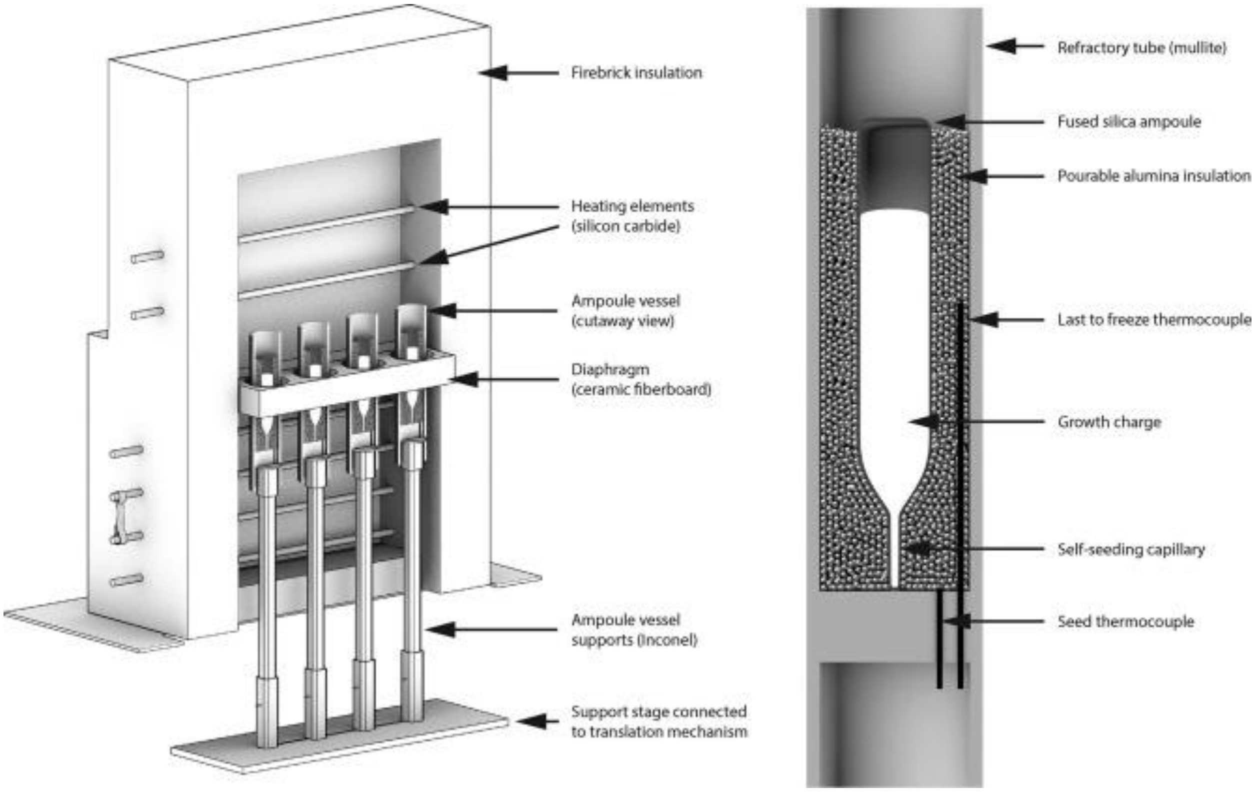

Figure 9: Cross section of the MAGS as prepared for growth of four crystals simultaneously. The growth ampoules are held in place by aluminum insulation, as shown on the right.

The sample is housed in a 150 ml Al_2O_3 crucible during the scan. The crucible is taken inside the glovebox, where a 30-50 mg section of crystal is measured out. The sample is then place inside the crucible, and loaded into the DSC, which is quickly closed and purged with argon gas. The DSC furnace has argon flowing during the length of the scan to prevent a reaction with moisture or oxygen. A typical heating profile will heat the sample at 5 °C/min up to ~50 °C above the melting temperature, and then cooled back to room temperature. This is done twice to remove any moisture from the sample as well as to ensure a good thermal contact for accurate temperature readings.

Powder X-ray Diffraction

The mixed halide samples were measured using powder X-ray diffraction for phase analysis. A piece of each of the five Ø15 mm $CsCaBr_xI_{3-x}$:Eu crystals was crushed in the glovebox then powdered using a mortar and pestle. Samples were loaded onto a silicon zero background plate, then covered with a Kapton film. The sample holder includes a round, plastic ring that crimps over the Kapton film, holding it in place and sealing the crystal from atmosphere during measurement. The zero-background plate, Kapton film, and sample holder are all then locked into a larger metal ring, shown in Figure 10.

The powder samples were measured at room temperature with a Panalytical Empyrean diffractometer in the Bragg-Brentano geometry. Cu K_α X-rays were generated at 45kV and 40 mA. Both incident beam and diffracted beam optics were the same as discussed in section 3.1. Each scan ran from 10-90° 2θ with a step size of 0.013° and total scan time of about 10 minutes. The sample holder was rotated at 30 rotations/minute to ensure detection of all crystallographic planes.

Optical Transmission

Optical transmission measurements were carried out to quantify the change in transparency as a result of the addition of bromine. 1 mm thick slabs were cut from the five Ø15mm samples and polished to a fine optical surface using 600, 800, and 1200 grit polishing pads and lapping oil. A varian cary 5000 Ev-Vis-NIR spectrophotometer was used to measure percent transmission over the range of 800-350 nm (1.5-4.2 eV). The sample holder consisted of a metal ring with two optical windows and an o-ring between them. The 1 mm slabs were loaded between the two windows inside the o-ring, and was submerged in mineral oil during the measurement. A custom tool was used to tighten a metal cap over the windows to seal in the oil and prevent the sample from sliding around during measurement. The sample holder was taped to a plastic stand that sits in the beamline. A baseline with no sample was measured, as well as a blocked-out beam for corrections, and the transmission is plotted as a percentage of the two extremes. Figure 11 is an image of the sample holder used for this measurement.

3.3.2 Scintillation properties

Radioluminescence and photoluminescence

Radioluminescence is the emission of light from a material when bombarded with ionizing radiation, and can be used to easily measure the emission spectrum for a scintillator. This is accomplished by using a PMT to measure the intensity at different wavelengths emitted by the crystal when excited with an X-ray source. A Cu target X-ray tube operated at 35 kV and 0.1 mA was placed directly in front of the sample. The five Ø15 mm slabs were contained in a clear polymer plastic bag and submerged in mineral oil during measurement. A 150 mm focal length monochromator and broadband PMT were used to collect insanity data over a 200-800 nm range.

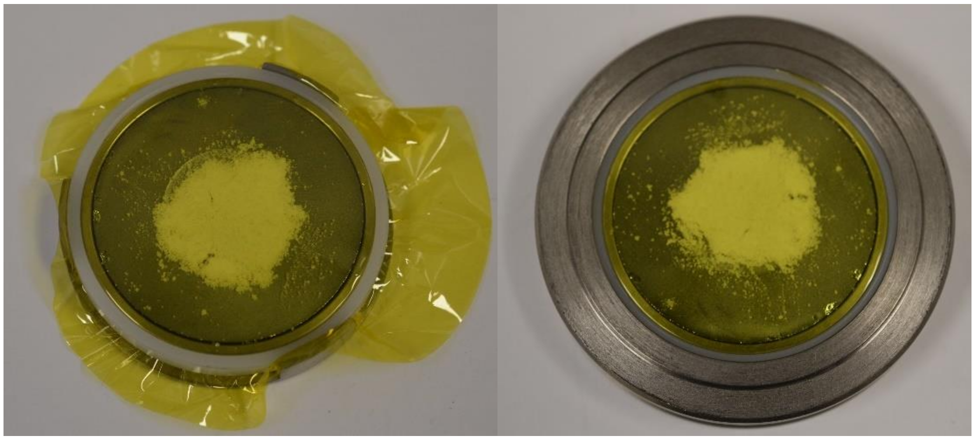

Figure 10: Powder XRD sample holder without (left) and with (right) outer sample holder with NaI powder loaded.

Figure 11: Sample holder (right) for transmission measurements and the tool for tightening it (left). The sample to be measured is protected by oil during the scan.

Scintillation utilizes ionizing radiation to create electron hole pairs, which recombine at activator sites. However, the activator sites themselves can be excited with lower energy photons that do not ionize the entire crystal. This is call photoluminescence, and it allows for analysis of solely the activator's optical properties. Photoluminescence was measured for the same five slabs with a Horiba Flourolog. A 4450W Xenon lamp was used to generate light in the visible spectrum, and a Hamamatsu R928 PMT collected the emission light. Excitation and emission spectra were collected for each composition of $CsCaBr_xI_{3-x}$:Eu

Gamma Spectroscopy

Each crystal was characterized in terms of its gamma ray spectroscopy abilities. The set up used consisted of a PMT housed in a dark box and analyzing electronics. To calculate absolute scintillation light yield, small size crystals were coated in mineral oil and placed directly onto a Hamamatsu R2059 PMT and covered with a Spectralon dome to collect the maximum number of photons. The PMT was biased at 1500 V and a ^{137}Cs source was used for excitation. The measured channel number of the 662 keV photopeak was compared to the single photoelectron response of the PMT, and corrected for the quantum efficiency of the PMT using the Radioluminescence spectrum.

To prevent degradation during remaining measurements, samples were housed in an oil cell that consists of a quartz ring glued to an optical window. Energy resolution and scintillation decay time measurements were measured on a Hamamatsu 6231-100 PMT operated at 1000 V. 38 mm crystals were measured using a Hamamatsu 6233 PMT operated at 1000 V. Oil cells were coupled to the PMT with mineral oil, then covered with Teflon tape. A ^{137}Cs source was used as the excitation source to measure the energy resolution at the 662 keV photopeak. The signal from the PMT was processed using a Canberra model 2005 pre-amplifier, an ORtec 672 amplifier, and a Tukan 8K muti-channel analyzer. Scintillation decay time was measured by analyzing the PMT signal directly via a Agilent InfiniiVision DSO6104A Digital Storage Oscilloscope. A single exponential was fit on an average of 128 scintillation pulses.

Chapter 4
Results and Discussion

4.1 Crystal Structure and Thermal Expansion of $CsCaI_3$:Eu

Before tweaking the composition of $CsCaI_3$:Eu, it was imperative that we understood the structure and the phase changes it undergoes. High temperature powder X-ray diffraction allows for the viewing of the change in crystal structure as a result of a temperature change, as well as the calculating of thermal expansion coefficients. Figure 12 shows the powder XRD patterns for $CsCaI_3$:Eu for temperatures both below and above the phase transition temperature (~250 °C). The left image shows the peaks for the entire scan range, while the right image highlights a region that allows for quick analysis of the phase change. The room temperature scan is consistent with the reported phase for $CsCaI_3$:Eu. The scans taken at 225 °C and below show four different peaks in the 28-30 °2θ region, while scans taken at 250 °C and above show only two peaks. Additionally, a minor peak at ~27 °2θ disappears above the phase transition temperature.

The combination of peaks around 29 ° and the loss of the 27 ° peak indicate a transition from a structure of low symmetry to a structure of high symmetry. Using GSAS II to conduct a phase search, a tetragonal structure with space group P 4/ b m and lattice parameters of a= 8.72 Å and c= 6.16 Å was found to be the best match. GSAS II was also used to determine the lattice parameters at each temperature for both phases. These, along with linear fits corresponding to the coefficient of thermal expansion (CTE), are plotted vs temperature in Figure 13. All parameters were found to increase linearly with temperature except the b parameter of the low temperature phase. Since both phases of $CsCaI_3$:Eu are right angle cells, the unit cell volume is simply the product of the three lattice parameters. The volumes for each temerature are plotted in Figure 14, along with a linear fit. It can be seen that the volume of the unit cell is cut nearly in half after the phase transition, with coresponds with the increase in symetery for the high temperature phase The volumeteric thermal expansion was calculated by the following equation:

$$\beta = \frac{1}{V}\frac{\Delta V}{\Delta T} = \alpha_a + \alpha_b + \alpha_c \tag{6}$$

where α_i corresponds to the linear thermal expansion for the i lattice parameter. The calculated values of linear thermal expansion and average volumetric expansion, as well as the ratios between the CTE's are compiled in Table 2. The thermal expansion coefficient of the b lattice parameter for the low temperature phase was not calculated, due to its lack of linear variation with temperature. The orthorhombic phase has a high value of CTE for the c lattice parameter, nearly double the value for the a lattice parameter. This anisotropic behavior is unfavorable for crystal growth, especially in a confined ampoule such as used in Bridgman growth. However, the tetragonal phase has a much small CTE for the c lattice parameter, and it is only 2% greater than the a lattice parameter. Although this is observed at high temperatures, it is possible that a similar tetragonal phase at room temperature would have similar behavior.

4.2 Optimizing bromine concentration

4.2.1 Crystal Growth

As mentioned in section 2.3, the bromine concentrations x= 0.2-1 were chosen to maintain the spectroscopic properties of $CsCaI_3$:Eu, while attempting to achieve a more favorable room temperature crystal structure. Four crystals were grown simultaneously to remove the effect of growth variations on

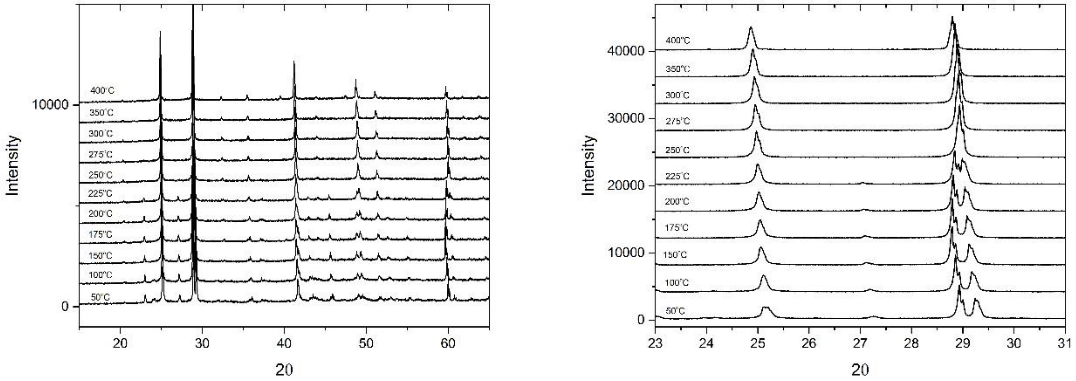

Figure 12: Powder XRD scans for $CsCaI_3$:Eu for the entire range (left) and a close up on a region of interest (right). The orthorhombic phase can be seen at temperatures below 250°C, while a tetragonal phase is observed above this temperature.

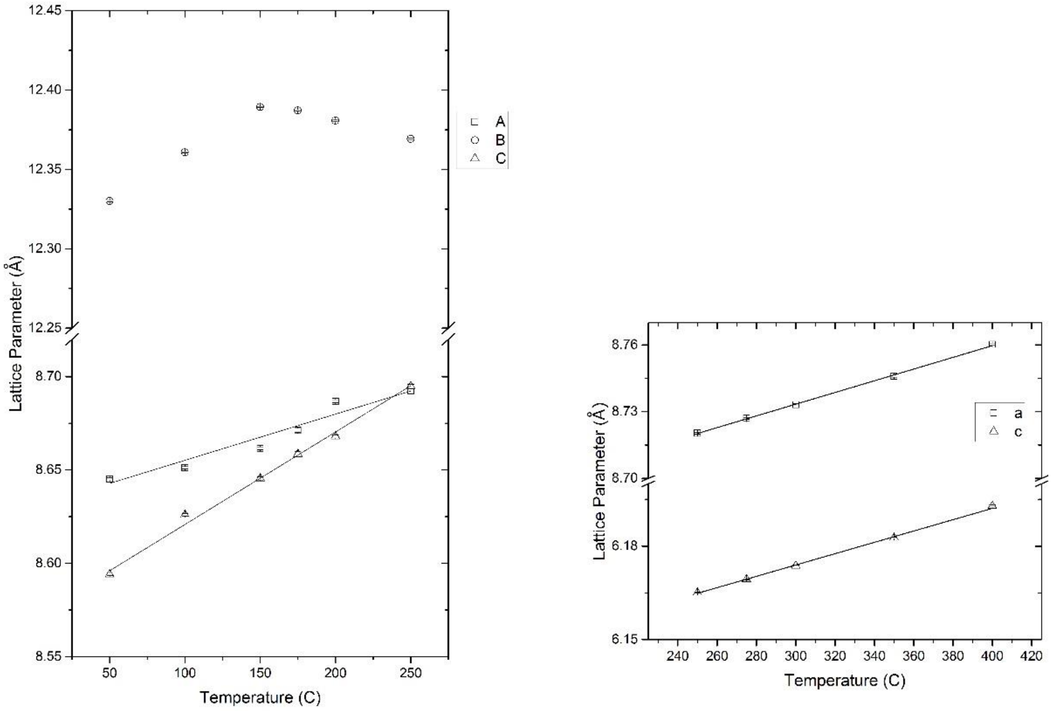

Figure 13: Lattice parameters and linear fits for the low temperature and high temperature phases of $CsCaI_3$:Eu.

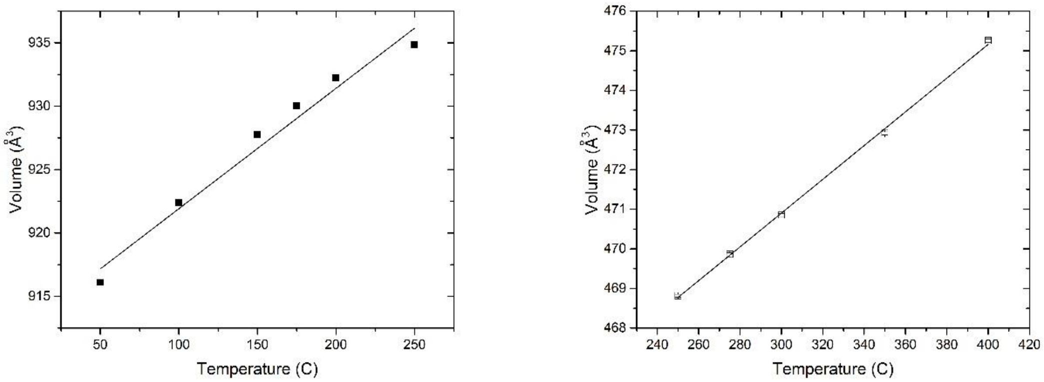

Figure 14: Unit Cell volume and linear fits for the low and high temperature phases of $CsCaI_3$:Eu.

Table 2: Linear and volumetric thermal expansion coefficients for CsCaI₃:Eu, as well as SrI₂:Eu and LaBr₃:Ce

Crystal	$\bar{\alpha}_a$ (10^{-5} K^{-1})	$\bar{\alpha}_b$ (10^{-5} K^{-1})	$\bar{\alpha}_c$ (10^{-5} K^{-1})	$\bar{\alpha}_V$ (10^{-5} K^{-1})	$\bar{\alpha}_a/\bar{\alpha}_b$	$\bar{\alpha}_a/\bar{\alpha}_c$	$\bar{\alpha}_b/\bar{\alpha}_c$
$CsCaI_3$:Eu Orthorhombic	3.61	N/A	6.94	11.2	-	0.52	-
$CsCaI_3$:Eu Tetragonal	3.02	-	2.95	9.00	-	1.02	-
SrI_2:Eu [47]	2.5	-	1.1	-	-	2.3	-
$LaCl_3$:Ce [48]	1.55	2.16	0.92	4.66	0.7	1.7	2.3

optical quality and scintillation performance. The fifth crystal (x=1) was grown with the same parameters and the possibility of growth variations was kept in mind when analyzing the grown crystals. The five Ø15 mm as-grown crystals are pictured in Figure 15. The thin section of the ampoule towards the bottom of the image are the self-seeding capillaries. All 5 crystals seeded correctly and yielded single crystals. Only the x=0.6 crystal showed moderate cracking, which is believed to appear during the cool down, not as an artifact of growth. To better acess the quality of the growth crystals, each was removed from its ampoule inside of the drybox and polised to remove surface rougness. The x=1 crytal had an especially rough surface, including snowflake-like crystalites, which can be seen in Figure 15. Figure 16 shows the crystals as removed and polished. It can now be seen that the x=0.4 and 0.8 crystals both have defect cores, starting around the cone section. This is most comonly caused by a concave interface during growth. The x=1 crystal developed a defect rich last-to-freeze region, possibly due to an interface breakdown towards the end of growth. A 5 mm slab was cut from the cone section of each crystal due to the uniform crystal quality across all samples, except for the cracked, x=0.6 crystal. These slabs are also included in Figure 16.

The cut, polished cone slabs reveal more about the optical quality of each composition. The crystals with $x < 0.6$ have a cloudy appearance similar to $CsCaI_3$:Eu, while the crystals with $x > 0.6$ are transparent. The imperfections seen on the x = 0.8 & 1 slabs are surface scratches, and not indicative of the overall crystal quality. The slab for x = 0.6 shows the cracks that developed throughout the crystal. As mentioned above, the defect cores are believed to be the result of a concave growth interface. One such cause is the development of a growth interface inside of the cold zone. To determine where the growth interface existed during growth, the melting temperature of each composition was measured using DSC scans. The resulting melting temperature of these crystals, as well as $CsCaI_3$:Eu are plotted vs bromine concentration in Figure 17. As the bromine concentration of the crystal increases, the melting temperature decreases nearly linearly. As the furnace temperatures were optimized for growth of $CsCaI_3$:Eu, the x= 0.2 crystal was able to grow without inclusions. However, the $x > 0.4$ crystals grown in MAGS developed solid-liquid interfaces lower in the furnace due to their suppressed melting temperatures.

4.2.2 Characterization

Structure Analysis

Due to the change in composition corresponding with an increase in Goldschmidt tolerance factor, the scans were taken for each of the five Ø15 mm crystals. The resultant patterns are compared in Figure 18. The bromine concentration starts at x = 0.2 at the bottom increases each pattern up. This measurement revealed the different structures for the different optical quality crystals. The lowest two bromine crystals have the same orthorhombic phase as $CsCaI_3$:Eu at room temperature, while the two highest bromine concentration crystals have a more symmetrical tetragonal phase. The median, x = 0.6 phase appears to have a combination of the two phases, which explains the cracked crystal quality. The different thermal expansion coefficients for the two phases induced stress in the boule upon cooling.

The complete high temperature structure analysis was not carried out for these five compositions. However, the phase transition temperature can be examined using DSC. The plot in Figure 19 highlights the changing phase transition temperature with regards to increasing bromine concentration via the exothermal peaks on the heating scan. The phase transition temperature in $CsCaBr_{0.2}I_{2.8}$:Eu occurs ~30 °C below the phase transition of $CsCaI_3$:Eu, while no phase transition was observed in $CsCaBr_{0.8}I_{2.2}$:Eu. It follows that as the Goldschmidt tolerance factor decreases, less energy is required to complete the

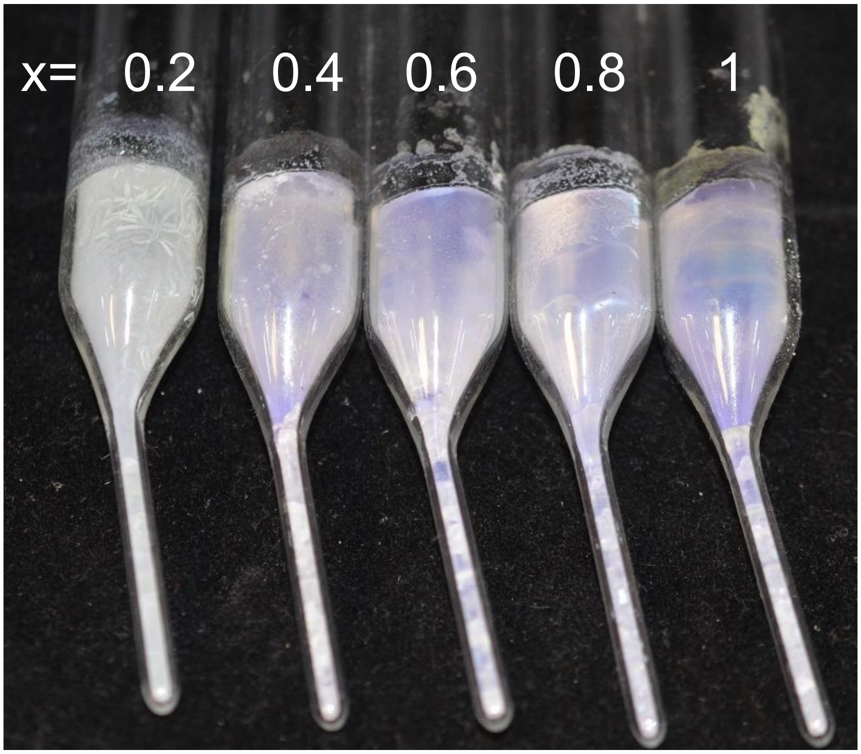

Figure 15: The five single crystal $CsCaBr_xI_{3-x}$*:Eu crystals still in growth ampoules.*

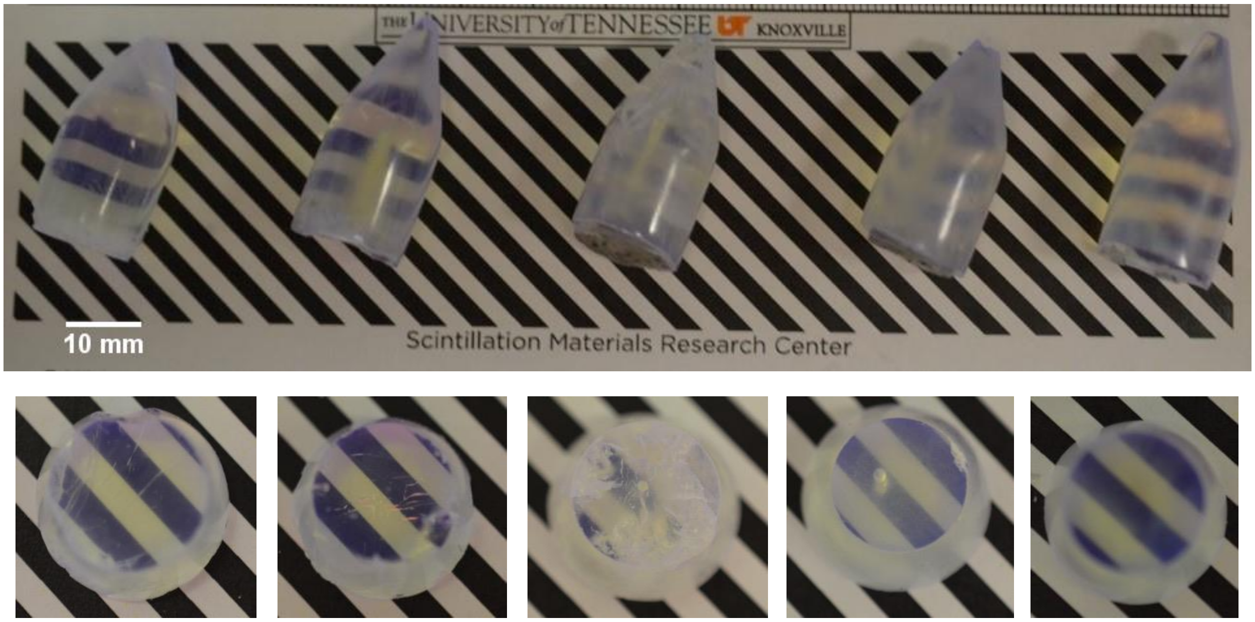

Figure 16: Crystals as removed from their ampoules and polished (above) and 5 mm slabs cut from their cone regions. The samples of the left have the highest bromine and the best optical quality, while the samples on the right have the lowest bromine and are less transparent.

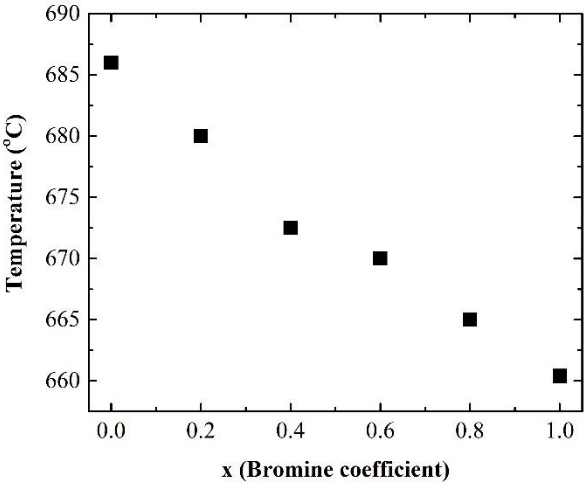

Figure 17: Melting temperature of $CsCaBr_xI_{3-x}$*:Eu as measured with Differential Scanning Calorimetry.*

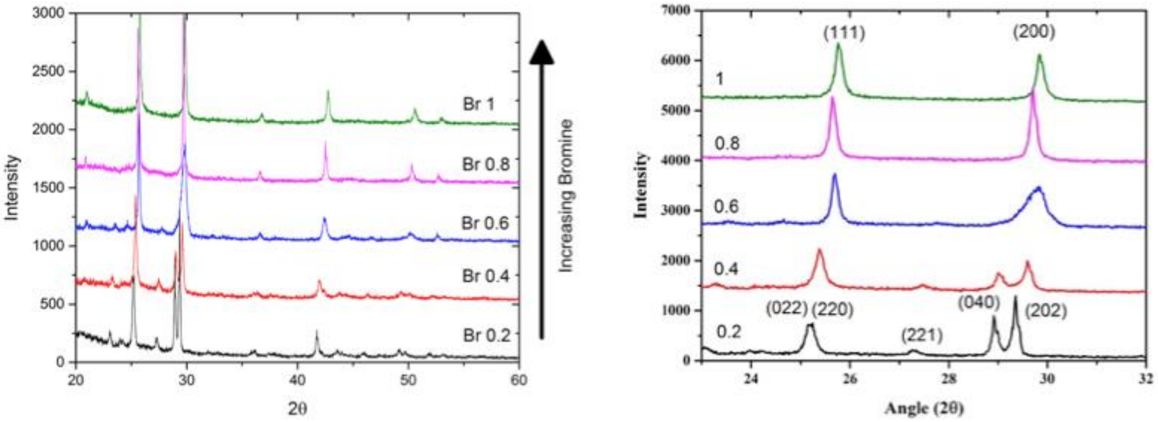

Figure 18: Powder XRD patterns for the five CsCaBr$_x$I$_{3-x}$:Eu crystals (left) and a zoomed in region of interest (right).

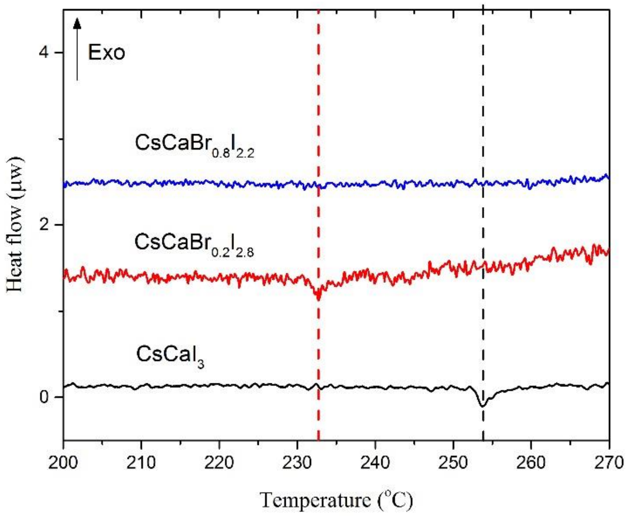

Figure 19: DSC heating scans of CsCaBr$_x$I$_{3-x}$:Eu highlighting the phase transition suppression with increased bromine. As bromine is substituted into CsCaI$_3$:Eu, the phase transition temperature decreases.

transition from orthorhombic to tetragonal, and at compositions above x = 0.6 the transition is suppressed below room temperature. It is not immediately clear whether the improved crystal quality results from the change in phase structure, or the removal of the phase transition. However, anecdotical evidence from transparent furnace growth of $CsCaI_3$:Eu (transparency at temperatures above 250 °C) supports the hypothesis that the cloudiness is a result of stress due to the phase transition.

To compare the optical quality differences between the two phases, the x = 1 and x = 0.2 boules were polished and imaged in Figure 20. The cloudiness of the $CsCaI_3$:Eu phase can be best highlighted by looking at the blurriness of the black lines on the imaging paper through the left crystal. The tetragonal phase has nearly perfect optical transparency, with only a small amount of inclusions seen in the top half of the boule on the right. To better quantify the change in optical quality, transmission was measured on the 1 mm thick slabs from each crystal. The 2 mm diameter pin hole for the measurement was aligned to an unincluded region of each slab, except for the cracked x= 0.6 crystal. The results of this experiment are presented in Figure 21. The transmission percentage decreases with increasing bromine, except for the x = 0.6 crystal, which can be attributed to the poor crystal quality of this composition. Additionally, the energy of the optical absorption edge slightly increases as bromine is added, which corresponds to an increase in the band gap. There is a slight difference in the slope of the transmission in the 1.5-2.5 eV range for the orthorhombic and tetragonal phases for which the mechanism is not explored in this work.

Scintillation properties

Although the optical quality of $CsCaI_3$:Eu was significantly improved via the substitution of iodine for bromine, improving scintillation performance is the ultimate goal of this work. The X-ray and optical emission, light yield, scintillation decay time, and gamma ray spectroscopy were accessed to determine the optimal bromine concentration. The emission profiles are plotted in Figure 22. The radioluminescence was unchanged for the five different compositions, as was the optical excitation and emission spectrum. Both the Radioluminescence and photoluminescence show emissions comparable with other Eu^{2+} doped scintillations, which is consistent with the 4d-5f transition. Because the photoluminescence profiles are the same, there will be no difference in self-absorption between the original and bromide compositions. However, the improvement in optical quality will reduce the optical scattering inside of the crystal, thereby reducing the photon path length and probability of self-absorption.

The gamma spectroscopy for each slab was analyzed using a ^{137}Cs source. The spectrum collected for the x = 1 slab is plotted in Figure 23. The energy resolution was measured in OriginPro 2017 with a single Gaussian fit of the 662 keV full energy deposition peak. The same resolution was measured for each of the five slabs. Additionally, the light yield of each of the slabs was measured and corrected for the quantum efficiency of the PMT using the Radioluminescence spectrum as well as the single photoelectron response. The relative light yield and energy resolution at 662 keV for all five compositions is visualized in Figure 24. The light yield decreases nearly linearly with added bromine concentration, while the energy resolution drops with added bromine but levels out above x = 0.6. The overall scintillation and physical properties for the five crystal slabs is summarized in Table 3. The absolute light yield of the lowest bromine slab is slightly improved compared to the published 40,000 photons/MeV of $CsCaI_3$:Eu. Although the light yield decreases with added bromine, the lowest measured value is only ~10% less than $CsCaI_3$:Eu. Additionally, the decay time is slightly reduced in the

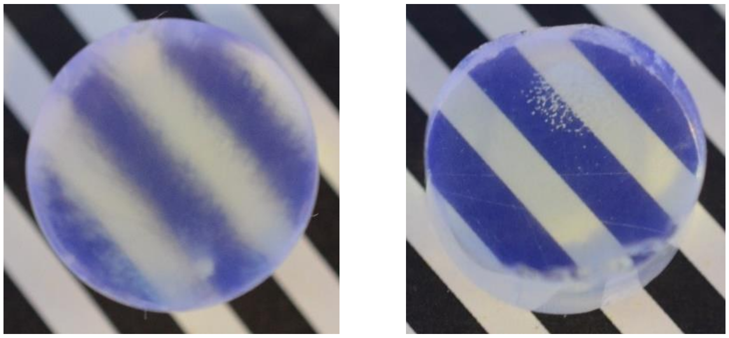

Figure 20: 15 mm thick boules of $CsCaBr_{0.2}I_{2.8}$*:Eu (left) and* $CsCaBrI_2$*:Eu. The optical quality of the higher bromine sample is much improved over the lower bromine sample.*

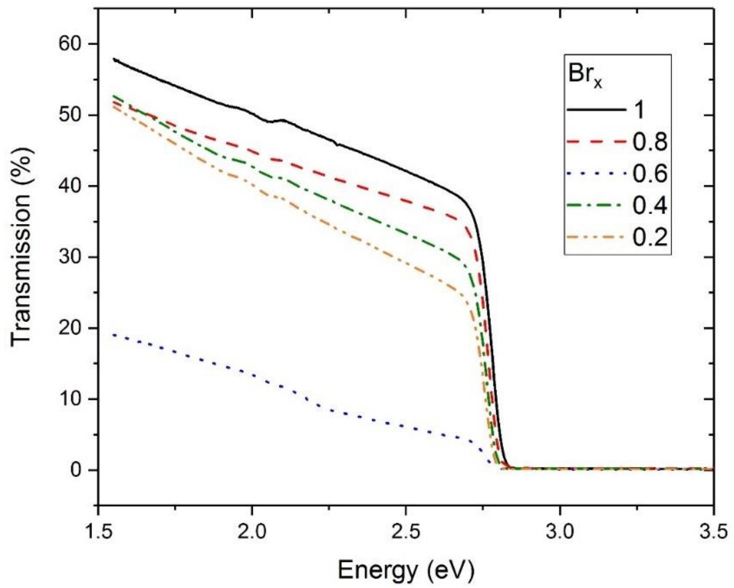

Figure 21: Transmission measurement for 1 mm thick slabs of $CsCaBr_xI_{3-x}$. The value shown in the figure legend represents the brome coefficient in the chemical composition.

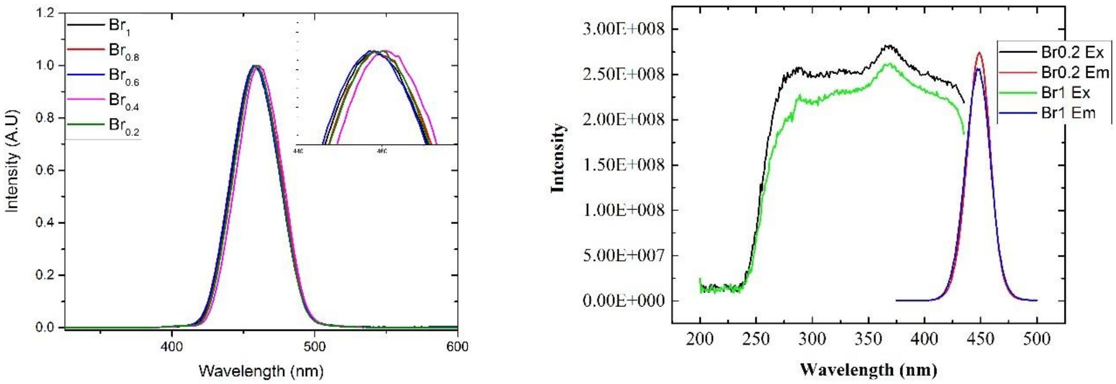

Figure 22: Radioluminescence of the five CsCaBr$_x$I$_{3-x}$:Eu slabs (left) and Photoluminescence of the two end point crystals (right).

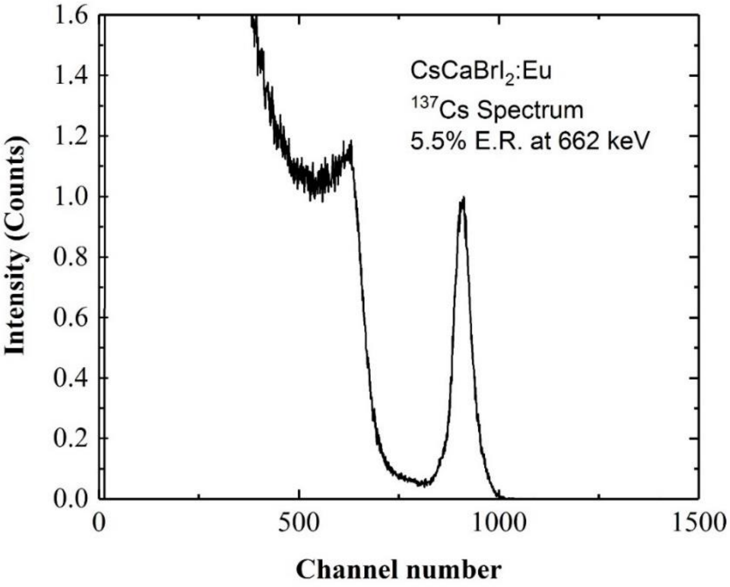

Figure 23: ^{137}Cs Spectrum measured with the CsCaBrI$_2$:Eu slab.

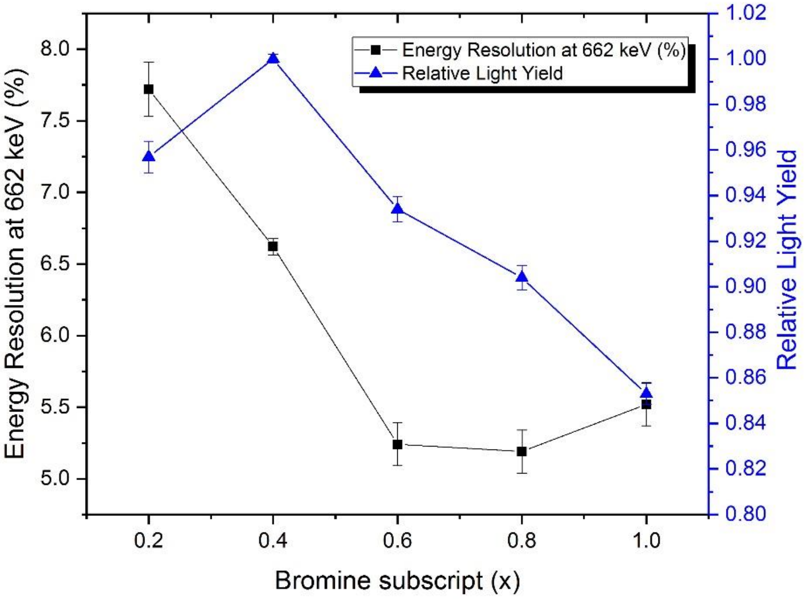

Figure 24: Light yield and energy resolution at 662 keV as measured on the cone slabs for each composition.

Table 3: Physical properties ad scintillation performance for the five $CsCaBr_xI_{3-x}$:Eu slabs

Br	Melting Point	Scintillation Light Yield	E.R. at 662 keV	Phase Structure	Scintillation Decay Time
0.2	680 °C	42,000 ph/MeV	7.3%	Orthorhombic	2.75 µs
0.4	673 °C	44,000 ph/MeV	6.6%	Orthorhombic	2.65 µs
0.6	670 °C	41,000 ph/MeV	5.3%	Mixed	2.32 µs
0.8	664 °C	40,000 ph/MeV	5.2%	Tetragonal	2.29 µs
1	660 °C	36,000 ph/MeV	5.5%	Tetragonal	2.25 µs

higher bromine concentration samples. From these values, the concentration $CsCaBr_{0.8}I_{2.2}$:Eu was chosen due to its improved energy resolution and optical quality, while not sacrificing a high light yield.

4.3 Growth of large size $CsCaBr_{0.8}I_{2.2}$:Eu

As seen in the previous section, $CsCaBr_{0.8}I_{2.2}$:Eu was chosen as the optimal concentration with an improved light yield and little trade off in terms of absolute light yield. However, for the application of national security gamma detection, the material must be producible at larger sizes. A 1 inch diameter crystal was grown in a vertical Bridgman furnace at 0.5 mm/hr. The ampoule for this crystal utilized an interior carbon coating to prevent crystal interactions with the quartz ampoule, which has been observed in other metal halide compositions. These interactions have the potential to create cracking due to stresses upon cooling, and increase the difficulty of sample preparation post growth. Additionally, a europium concentration of 2 molar percent was chosen to mitigate self-absorption at larger sizes. The full boule of the grown crystal, minus the cone and last-to-freeze region is shown in Figure 25, alongside a 1 cm^3 cube cut from it.

The cube and the bulk of the crystal are extremely transparent, as expected from the previous experiment. However, the ~ 2 mm thick region on the outside of the sample was heavily cracked. This region can easily be broken off the crystal with a pair of forceps. It is possible that a convex growth interface led to segregation of a certain phase or impurity to the outside of the crystal as opposed to the last-to-freeze region. Since the crystal was grown in a carbon coated ampoule, the shape of the solid-liquid interface is unknown. However, previous work on Si_xGe_{1-x} has shown that a convex growth interface can lead to changes in crystal composition near the perimeter of the crystal [49]. To test for this, a 1 mm slab was cut from the remainder of the boule. Powder XRD scans were taken of samples from both the perimeter and the center of this slab. The peaks for these samples are compared in Figure 26 along with the XRD scan taken for the $CsCaBr_{0.8}I_{2.2}$:Eu crystal grown in section 4.2.

The bottom two patterns, the standard and the center of the Ø1 ” crystal, have very similar peaks, while the cracked edge of the Ø1 ” crystal shows extra peaks. These peaks did not fit with $CsCaI_3$, $CsCaBr_3$, or any of the starting components. Additionally, because the lack of shifting between the uncracked samples, it is unlikely that the 1” crystal segregated large amounts of iodine or bromide compared to the Ø15 mm crystal. The nature of this perimeter impurity phase is unknown at this time. The 1 cm cube of this crystal was characterized for its gamma spectroscopy abilities, and the recorded ^{137}Cs spectrum is plotted in Figure 27. The overlaid red curve shows the best gaussian fit. Due to the asymmetry of the full energy peak, only a portion of the peak was fit. This peak shape is possibly due to the cube geometry of the measured sample.

To prevent the cracking resulting from a convex growth interface, the next crystals were grown in a transparent furnace with a uncoated quartz ampoule. This allowed for visual inspection while adjusting the top and bottom zone temperatures until the desired interface was achieved. A Ø22 mm crystal of composition $CsCaBr_{0.8}I_{2.2}$:Eu 5% was prepared and synthesized at 800° C. The growth was accomplished with a translation rate of 0.5 mm/hr and a cooling rate of 7 °C/hr. The resulting crystal was nearly flawless, with a ~1 mm wide crack along the perimeter of the boule. The crystal as removed from the ampoule is featured in Figure 28. The transparency of the crystal allows for a clear look at the roughness on its surface. This is an artifact of growth, and is polished off with moderate ease. A 24 mm tall cylinder was cut from the crystal and polished, and is pictured in Figure 29. The lone crack in the crystal can be seed just left of the scale bar on the image.

Figure 25: Full boule of $CsCaBr_{0.8}I_{2.2}$:Eu 2% (left) and a 1 cm cube sourced from the crystal.

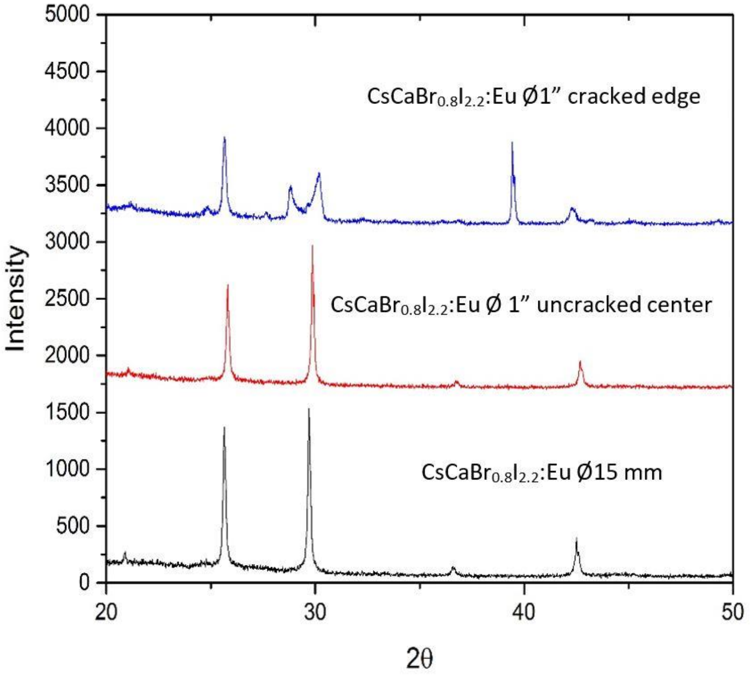

Figure 26: Powder XRD spectrum for the cracked and uncracked regions of the 1" crystal. There is an unknown phase present in the cracked edge of the crystal.

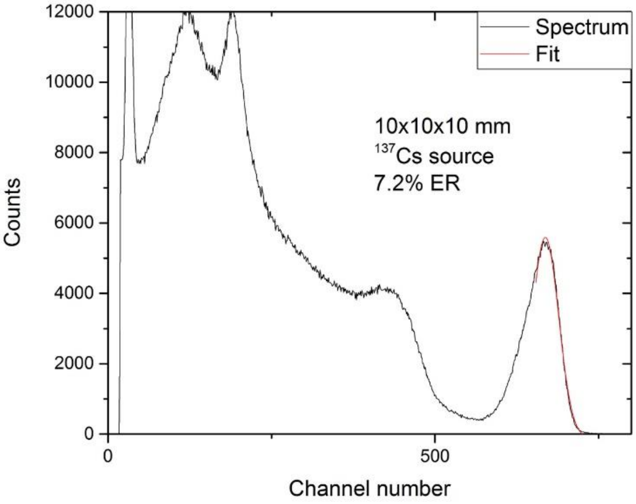

Figure 27: ^{137}Gamma spectrum of the 1 cm cube cut from $CsCaBr_{0.8}I_{2.2}$:Eu.

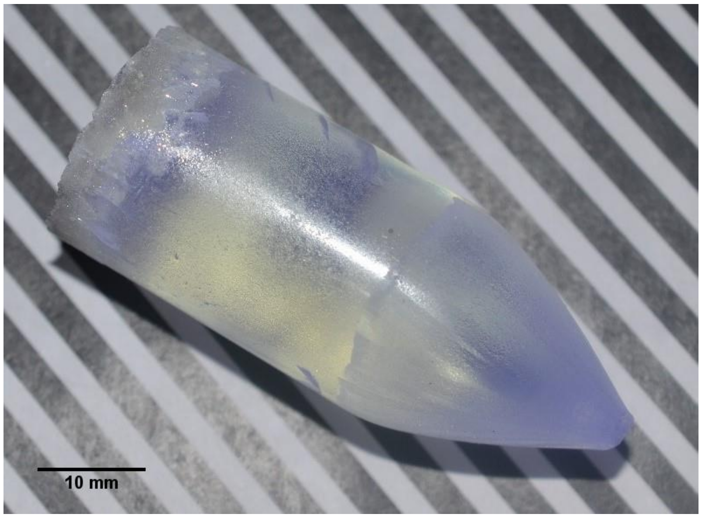

Figure 28: Ø22 mm $CsCaBr_{0.8}I_{2.2}$*:Eu crystal as removed from the growth ampoule. The rough surface texture is easily polished away.*

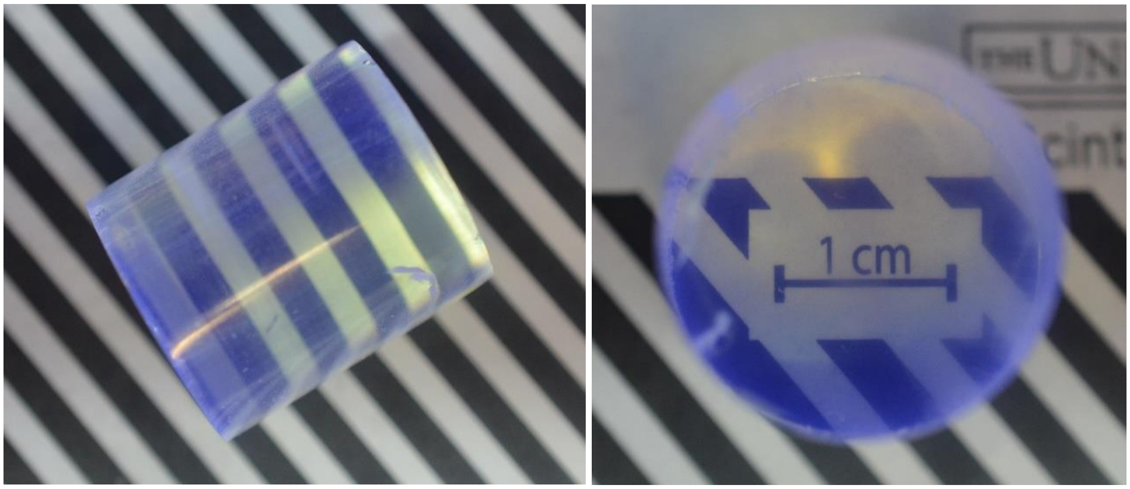

Figure 29: Cut and polished boule of $CsCaBr_{0.8}I_{2.2}$*:Eu grown in a transparent furnace.*

The 24 mm tall boule was measured for its gamma spectroscopic abilities using a ^{137}Cs source. As one of the goals of this work was to improve the performance of $CsCaI_3$:Eu, a $CsCaI_3$:Eu boule measuring Ø22 x 12mm was measured in the same fashion. Both of these spectra are plotted in Figure 30, with the normalized energy on the x-axis. The $CsCaBr_{0.8}I_{2.2}$:Eu is clearly the better performer, with an energy resolution of 8.4% at 662 keV vs 11.2% at 662 keV for $CsCaI_3$:Eu. Furthermore, this boule was double the volume of the $CsCaI_3$:Eu, which suffers severely from performance deterioration with size, as shown in Figure 6. The energy resolution of 8.4% at 662 keV is slightly worse than that measured on the previous 1 cm cube (7.2% at 662 keV). This is to be expected, as the volume increased tenfold from 1 cm^3 in the cube to 10.86 cm^3 in the cylindrical boule. Because the small size samples were not drastically improved as compared to $CsCaI_3$:Eu at similar sizes, the improvement in energy resolution in larger sizes can be attributed to the improved optical quality of $CsCaBr_{0.8}I_{2.2}$:Eu. There is significantly less scattering of optical photons in the improved composition, as can be seen in photographs. The reduction in photon scattering also reduces the average photon path length in the crystal. Because self-absorption is a probabilistic effect, the shorter that the scintillation photons travel in the bulk of the crystal, the less chance they have of becoming self-absorbed.

The Ø22 mm crystal was also measured using a columnated ^{137}Cs source. The crystal was contained in an oil cell and mounted to the PMT with optical grease. Two lead bricks were used to create a fan shaped beam from the ^{137}Cs source. The beam was focused on the top ~ 5 mm of the crystal. The measured spectrum and gaussian fit are plotted in Figure 31. The energy resolution of the boule when using a columnated gamma source is reduced from 8.4% to ~5% at 662 keV. The improvement in energy resolution corresponds to the lack of variation in gamma interaction locations. Due to the specific location of the beam, there is only a difference in interaction in the radial direction, which is highly symmetric. The uncollimated beam allows for energy deposition across the entire boule, where the activator concentration varies due to segregation during growth.

Due to the successful growth of $CsCaBr_{0.8}I_{2.2}$:Eu at Ø22 mm, a Ø38 mm crystal was grown in identical conditions. The solid-liquid interface was maintained flat throughout the entire growth. The crystal, as polished out of the boule, is pictured in Figure 32. Surface cracks can be seen on the last-to-freeze and cone section of the otherwise transparent crystal. A 34 mm tall slab was cut from the boule, and is also pictured in Figure 32. The cracks along the perimeter of the boule were a product of the mounting and cutting process. The crystal was measured with a ^{137}Cs source, and the resulting spectrum is plotted in Figure 33. The measured energy resolution of 9.5% at 662 keV is a significant improvement over the 13% at 662 for similar sized $CsCaI_3$:Eu. Additionally, the peak shape is more symmetrical for $CsCaBr_{0.8}I_{2.2}$:Eu. This is most likely due to the intrinsic resolution of the composition, while the resolution of $CsCaI_3$:Eu is greatly affected by light collection effects, especially at large sizes.

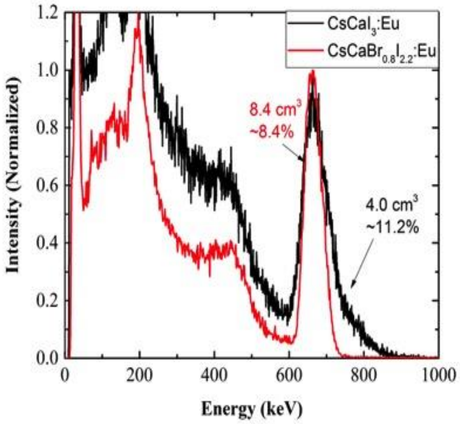

Figure 30: CsCaBr$_{0.8}$I$_{2.2}$:Eu and CsCaI$_3$:Eu performance at 22 mm diameter, labeled with crystal volume and energy resolution. The optimized concentration crystal shows a better energy resolution at double the volume of a CsCaI$_3$:Eu boule.

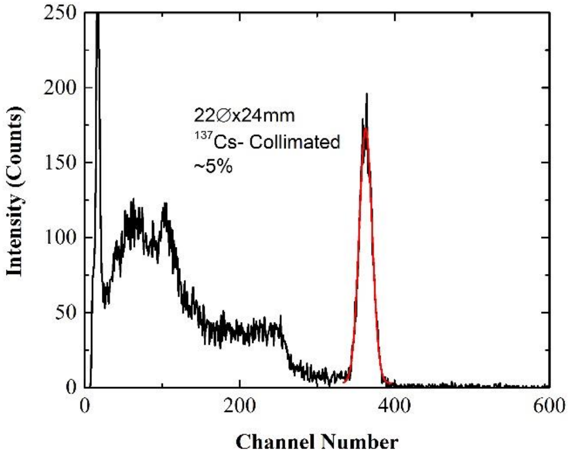

Figure 31: Gamma Spectrum of $CsCaBr_{0.8}I_{2.2}$*:Eu measured with a collimated* ^{137}*Cs source. The energy resolution is improved when only a 5 mm thickness of the boule is irradiated.*

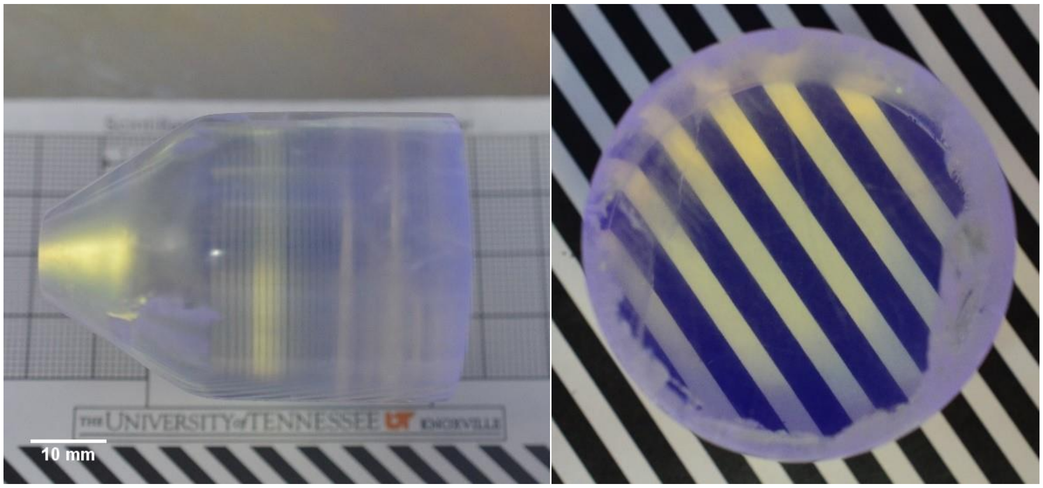

Figure 32: Ø38 mm $CsCaBr_{0.8}I_{2.2}$*:Eu crystal full boule (left) and 34 mm tall cylinder (right). The cut crystal shows only minor surface cracking.*

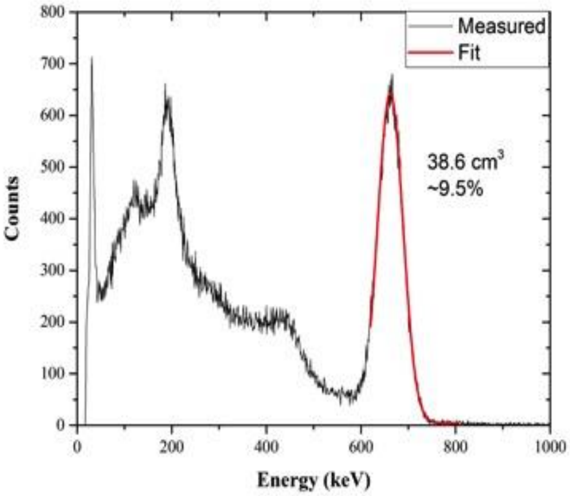

Figure 33: ^{137}Cs Spectrum of the Ø38 mm CsCa$Br_{0.8}I_{2.2}$:Eu crystal. Crystal volume and energy resolution are shown next to the full energy peak.

Chapter 5
Conclusions

In this work we set out to improve the scintillator composition $CsCaI_3$:Eu. High temperature X-ray diffraction studies revealed the nature of the solid-to-solid phase transition it undergoes upon cooling. Based on the ratio of ionic radii of elements in the material as well as knowledge of the composition $CsCaBr_3$:Eu led to the decision to substitute some of the iodine in $CsCaI_3$:Eu with bromine to create a new composition, $CsCaBr_xI_{3-x}$:Eu. The optimal bromine x value was determined using an investigative crystal growth of five different compositions. It was found that the structure of $CsCaBr_xI_{3-x}$:Eu becomes similar to that of high temperature $CsCaI_3$:Eu when the bromine x value is above 0.6. After comparing different physical and scintillation properties of the five compositions, $CsCaBr_{0.8}I_{2.2}$:Eu was chosen to be grown at large sizes, is as needed for national security applications.

$CsCaBr_{0.8}I_{2.2}$:Eu was grown at both 22 and 38 mm diameter successfully. The Ø22 mm crystal yielded a stronger energy resolution at 662 keV than a similar width but half as tall $CsCaI_3$:Eu. This crystal was able to reach 5% energy resolution at 662 keV when excited with a collimated ^{137}Cs source. The Ø38 mm crystal was nearly uncracked and highly transparent. A 38.6 cm^3 slab cut from this crystal reached 9.5% energy resolution at 662 keV, a significant improvement over >11% for $CsCaI_3$:Eu of similar sizes. This research has highlighted usefulness of tweaking the composition of perovskite materials in order to change their room temperature structures. Additionally, we have discovered a new scintillator composition with performance comparable to that of NaI in all regards except decay time, at sizes large enough for national security gamma and X-ray detection applications.

List of References

[1] I. A. E. AGENCY, *IAEA Safeguards Glossary* (International Nuclear Verification Series, no. 3). Vienna: INTERNATIONAL ATOMIC ENERGY AGENCY, 2002.

[2] J. E. Turner, *Atoms, Radiation, and Radiation Protection*. Wiley, 2007.

[3] D. J. Robbins, "On Predicting the Maximum Efficiency of Phosphor Systems Excited by Ionizing Radiation," *Journal of the Electrochemical Society,* vol. 127, no. 12, 1980.

[4] A. Lempicki, A. J. Wojtowicz, and E. Berman, "Fundamental limits of scintillator performance," *Nuclear Instruments and Methods in Physics Research Section A: Accelerators, Spectrometers, Detectors and Associated Equipment,* vol. 333, no. 2, pp. 304-311, 1993/09/01 1993.

[5] P. Dorenbos, J. T. M. d. Haas, and C. W. E. v. Eijk, "Non-proportionality in the scintillation response and the energy resolution obtainable with scintillation crystals," *IEEE Transactions on Nuclear Science,* vol. 42, no. 6, pp. 2190-2202, 1995.

[6] P. Dorenbos, "Fundamental Limitations in the Performance of Ce^{3+} ,Pr^{3+} , and Eu^{2+} Activated Scintillators," *IEEE Transactions on Nuclear Science,* vol. 57, no. 3, pp. 1162-1167, 2010.

[7] G. F. Knoll, *Radiation detection and measurement*. New York: Wiley, 1979, pp. xv, 816 p.

[8] Ortec. *Detective-Remote Nuclear Threat Detection Software*. Available: http://www.ortec-online.com/products/nuclear-security-and-safeguards/mobile-detection-systems/detective-remote-software

[9] P. Lecoq, *Inorganic scintillators for detector systems : physical principles and crystal engineering* (Particle acceleration and detection). Berlin ; New York: Springer, 2006, pp. xii, 251 p.

[10] V. C. A. Yoshikawa, and M. Nikl, "Czochralski Growth and Properties of Scintillating Crystals," *ACTA Physica Polonica A,* vol. 127, no. 2, 2013.

[11] J. Valentine, D. Wehe, G. Knoll, and C. Moss, "Temperature dependence of absolute CsI(Tl) scintillation yield," in *Conference Record of the 1991 IEEE Nuclear Science Symposium and Medical Imaging Conference*, 1991, pp. 176-182 vol.1.

[12] S. Keszthelyi-Lándori and G. Hrehuss, "Scintillation response function and decay time of CsI(Na) to charged particles," *Nuclear Instruments and Methods,* vol. 68, no. 1, pp. 9-12, 1969/02/01 1969.

[13] N. J. Cherepy *et al.*, "Strontium and barium iodide high light yield scintillators," *Applied Physics Letters,* vol. 92, no. 8, p. 083508, 2008.

[14] A. Iltis, M. R. Mayhugh, P. Menge, C. M. Rozsa, O. Selles, and V. Solovyev, "Lanthanum halide scintillators: Properties and applications," *Nuclear Instruments and Methods in Physics Research Section A: Accelerators, Spectrometers, Detectors and Associated Equipment,* vol. 563, no. 2, pp. 359-363, 7/15/ 2006.

[15] E. D. Bourret-Courchesne, G. Bizarri, S. M. Hanrahan, G. Gundiah, Z. Yan, and S. E. Derenzo, "BaBrI:Eu2+, a new bright scintillator," *Nuclear Instruments and Methods in Physics Research Section A: Accelerators, Spectrometers, Detectors and Associated Equipment,* vol. 613, no. 1, pp. 95-97, 1/21/ 2010.

[16] W. M. Higgins, A. Churilov, E. van Loef, J. Glodo, M. Squillante, and K. Shah, "Crystal growth of large diameter LaBr3:Ce and CeBr3," *Journal of Crystal Growth,* vol. 310, no. 7–9, pp. 2085-2089, 4// 2008.

[17] A. C. Lindsey, M. Zhuravleva, L. Stand, Y. Wu, and C. L. Melcher, "Crystal growth and characterization of europium doped KCaI3, a high light yield scintillator," *Optical Materials,* vol. 48, pp. 1-6, 10// 2015.

[18] L. Stand, M. Zhuravleva, A. Lindsey, and C. L. Melcher, "Growth and characterization of potassium strontium iodide: A new high light yield scintillator with 2.4% energy resolution," *Nuclear Instruments and Methods in Physics Research Section A: Accelerators, Spectrometers, Detectors and Associated Equipment,* vol. 780, pp. 40-44, 4/21/ 2015.

[19] V. L. Cherginets *et al.*, "Scintillation properties of CsSrX3:Eu2+ (CsSr1−yEuyX3, X = Cl, Br; $0 \leq y \leq 0.05$) single crystals grown by the Bridgman method," *Materials Chemistry and Physics,* vol. 143, no. 3, pp. 1296-1299, 2/14/ 2014.

[20] L. Stand, M. Zhuravleva, B. Chakoumakos, J. Johnson, A. Lindsey, and C. L. Melcher, "Scintillation properties of Eu2+-doped KBa2I5 and K2BaI4," *Journal of Luminescence,* vol. 169, Part A, pp. 301-307, 1// 2016.

[21] P. W. Bridgman, "Certain Physical Properties of Single Crystals of Tungsten, Antimony, Bismuth, Tellurium, Cadmium, Zinc, and Tin," *Proceedings of the American Academy of Arts and Sciences,* vol. 60, no. 6, pp. 305-383, 1925.

[22] D. C. Stockbarger, "The Production of Large Single Crystals of Lithium Fluoride," *Review of Scientific Instruments,* vol. 7, no. 3, pp. 133-136, 1936/03/01 1936.

[23] C. E. Chang and W. R. Wilcox, "Control of interface shape in the vertical bridgman-stockbarger technique," *Journal of Crystal Growth,* vol. 21, no. 1, pp. 135-140, 1974/01/01 1974.

[24] T.-W. Fu and W. R. Wilcox, "Influence of insulation on stability of interface shape and position in the vertical Bridgman-Stockbarger technique," *Journal of Crystal Growth,* vol. 48, no. 3, pp. 416-424, 1980/03/01 1980.

[25] A. Yoshikawa *et al.*, "Growth of 2Inch Eu-doped SrI2 single crystals for scintillator applications," *Journal of Crystal Growth,* vol. 452, pp. 73-80, 2016/10/15/ 2016.

[26] K. Nishimoto, Y. Yokota, S. Kurosawa, K. Kamada, A. Ymaji, and A. Yoshikawa, "Eu concentration dependence on scintillation properties of Eu doped SrI2 single crystals grown by modified micro-pulling-down method," *Optical Materials,* vol. 36, no. 12, pp. 1946-1949, 2014/10/01/ 2014.

[27] L. Stand *et al.*, "Exploring growth conditions and Eu2+ concentration effects for KSr2I5:Eu scintillator crystals," *Journal of Crystal Growth,* vol. 439, pp. 93-98, 4/1/ 2016.

[28] A. Lindsey, "Material and Process Engineering for Bulk Single Crystal Growth of High Performance Scintillator Potassium Calcium Iodide," Ph.D., Materials Science and Engineering, University of Tennessee, 2016.

[29] J. Glodo, E. V. v. Loef, N. J. Cherepy, S. A. Payne, and K. S. Shah, "Concentration Effects in Eu Doped SrI<formula formulatype="inline"> <tex Notation="TeX">$_{2}$</tex></formula>," *IEEE Transactions on Nuclear Science,* vol. 57, no. 3, pp. 1228-1232, 2010.

[30] Y. Wu, M. Zhuravleva, A. C. Lindsey, M. Koschan, and C. L. Melcher, "Eu2+ concentration effects in KCa0.8Sr0.2I3:Eu2+: A novel high-performance scintillator," *Nuclear Instruments and Methods in Physics Research Section A: Accelerators, Spectrometers, Detectors and Associated Equipment,* vol. 820, pp. 132-140, 6/1/ 2016.

[31] A. C. Lindsey *et al.*, "Effects of increasing size and changing europium activator concentration in KCaI3 scintillator crystals," *Journal of Crystal Growth,* vol. 449, pp. 96-103, 9/1/ 2016.

[32] A. Lindsey, W. McAlexander, L. Stand, Y. Wu, M. Zhuravleva, and C. L. Melcher, "Crystal growth and spectroscopic performance of large crystalline boules of CsCaI3:Eu scintillator," *Journal of Crystal Growth,* vol. 427, pp. 42-47, 10/1/ 2015.

[33] M. Zhuravleva, B. Blalock, K. Yang, M. Koschan, and C. L. Melcher, "New single crystal scintillators: CsCaCl3:Eu and CsCaI3:Eu," *Journal of Crystal Growth,* vol. 352, no. 1, pp. 115-119, 8/1/ 2012.

[34] G. Schilling and G. Meyer, "Ternäre Bromide und Iodide zweiwertiger Lanthanide und ihre Erdalkali-Analoga vom Typ AMX3 und AM2X5," *Zeitschrift für anorganische und allgemeine Chemie,* vol. 622, no. 5, pp. 759-765, 1996.

[35] Y. Wang, F. Guyot, and R. C. Liebermann, "Electron microscopy of (Mg, Fe)SiO3 Perovskite: Evidence for structural phase transitions and implications for the lower mantle," *Journal of Geophysical Research: Solid Earth,* vol. 97, no. B9, pp. 12327-12347, 1992.

[36] A. Y. Grippa *et al.*, "Crystal growth and scintillation properties of CsCaBr3:Eu2+(CsCa1−xEuxBr3, 0≤x≤0.08)," *Journal of Crystal Growth,* vol. 371, pp. 112-116, 5/15/ 2013.

[37] V. M. Goldschmidt, "Die Gesetze der Krystallochemie," *Naturwissenschaften,* vol. 14, no. 21, pp. 477-485, 1926// 1926.

[38] R. C. Murty, "Effective Atomic Numbers of Heterogeneous Materials," *Nature,* 10.1038/207398a0 vol. 207, no. 4995, pp. 398-399, 07/24/print 1965.

[39] S. S. Gokhale, L. Stand, A. Lindsey, M. Koschan, M. Zhuravleva, and C. L. Melcher, "Improvement in the optical quality and energy resolution of CsSrBr3: Eu scintillator crystals," *Journal of Crystal Growth,* vol. 445, pp. 1-8, 7/1/ 2016.

[40] Y. Wu *et al.*, "Toward High Energy Resolution in CsSrI3/Eu2+ Scintillating Crystals: Effects of Off-Stoichiometry and Eu2+ Concentration," *Crystal Growth & Design,* vol. 16, no. 12, pp. 7186-7193, 2016/12/07 2016.

[41] L. Stand, M. Zhuravleva, H. Wei, and C. L. Melcher, "Crystal growth and scintillation properties of potassium strontium bromide," *Optical Materials,* vol. 46, pp. 59-63, 8// 2015.

[42] H. Wei, V. Martin, A. Lindsey, M. Zhuravleva, and C. L. Melcher, "The scintillation properties of CeBr3−xClx single crystals," *Journal of Luminescence,* vol. 156, pp. 175-179, 12// 2014.

[43] R. T. Poole, J. G. Jenkin, J. Liesegang, and R. C. G. Leckey, "Electronic band structure of the alkali halides. I. Experimental parameters," *Physical Review B,* vol. 11, no. 12, pp. 5179-5189, 06/15/ 1975.

[44] A. V. Gektin, A. N. Belsky, and A. N. Vasil'ev, "Scintillation Efficiency Improvement by Mixed Crystal Use," *IEEE Transactions on Nuclear Science,* vol. 61, no. 1, pp. 262-270, 2014.

[45] B. H. T. a. R. B. V. Dreele, "GSASII: the genesis of a modern open-source all purpose crystallography software packaged," *Journal of Applied Crystallography,* vol. 46, no. 2, pp. 544-549, 2013.

[46] A. C. Lindsey, Y. Wu, M. Zhuravleva, M. Loyd, M. Koschan, and C. L. Melcher, "Multi-ampoule Bridgman growth of halide scintillator crystals using the self-seeding method," *Journal of Crystal Growth,* vol. 470, pp. 20-26, 7/15/ 2017.

[47] N. J. Cherepy *et al.*, "SrI2 scintillator for gamma ray spectroscopy," 2009, vol. 7449, pp. 74490F-74490F-6.

[48] G. Meyer, "Thermal-Behavior Of Complex Halides," *Eur. J. Solid State Inorg. Chem.,* vol. 28, no. 6, pp. 1209-43, 1991.

[49] A. C. Wagner, A. Cröll, and H. Hillebrecht, "Si1−xGex crystal growth by the floating zone method starting from SPS sintered feed rods – A segregation study," *Journal of Crystal Growth,* vol. 448, pp. 109-116, 2016/08/15/ 2016.

Vita

Matthew Starr Loyd was born in Florida, but has spent his entire life past infancy in Tennessee. He was raised in Germantown, his residence through high school. In 2011 he moved east where received his Bachelors in Materials Science and Engineering in 2015 at the University of Tennessee, Knoxville. There, he met his fiancé Sydney, with whom he is a happy father to a Goldendoodle, Penny. Matthew was driven to engineering by his passion of math and building Legos, as well as his parents Jon and Mary, who always pushed him to succeed and instilled in him a love of knowledge. Outside of research, he enjoys sports, music, playing basketball, and taking walks with his dog and fiancé.